Cholesterol metabolism plays a crucial role in the regulation of autophagy for cell differentiation of granular convoluted tubules in male mouse submandibular glands

Akiko Suzuki[1,2], Junbo Shim[1,2], Kenichi Ogata[1,2], Hiroki Yoshioka[1,2], and Junichi Iwata[1,2,3,*]

[1]Department of Diagnostic & Biomedical Sciences, The University of Texas Health Science Center at Houston, School of Dentistry, Houston, Texas, USA

[2]Center for Craniofacial Research, The University of Texas Health Science Center at Houston, School of Dentistry, Houston, Texas, USA

[3]MD Anderson Cancer Center UTHealth Graduate School of Biomedical Sciences, Houston, Texas, USA

Competing financial interests: The authors declare no competing financial interests.

Correspondence to: Junichi Iwata. Correspondence and requests for materials should be addressed to J.I. (Email: Junichi.Iwata@uth.tmc.edu).

KEY WORDS: Cholesterol metabolism, Autophagy, Salivary glands, Differentiation, Duct formation

ABSTRACT

It has been long appreciated that sex-hormone receptors are expressed in various non-gonadal organs. However, it remains unclear how sex hormones regulate the morphogenesis of these non-gonadal organs. To address this question, we used a male mouse model of androgen-dependent salivary gland morphogenesis. Mice with excessive cholesterol synthesis in the salivary glands exhibited defects in the maturation of granular convoluted tubules (GCTs), which is regulated through sex hormone-dependent cascades. We found that excessive cholesterol synthesis resulted in autophagy failure specifically in the duct cells of salivary glands, followed by the accumulation of NRF2, a transcription factor known as one of the specific substrates for autophagy. The accumulated NRF2 suppressed the expression of *Foxa1*, which forms a transcriptional complex with the androgen receptor to regulate target genes. Taken together, our results indicate that cholesterol metabolism plays a crucial role in GCT differentiation through autophagy.

INTRODUCTION

Rodent submandibular glands (SMGs) are composed of acini and duct systems that contain intercalated ducts (IDs), striated ducts (SDs), granular convoluted tubules (GCTs), and excretory ducts (Pinkstaff, 1980). The GCTs are located between the IDs and SDs and develop from SDs with the onset of puberty, in an androgen-dependent manner, in male rodents (Dunn and Wilson, 1975). Therefore, rodent SMGs display morphological and functional sexual dimorphism (Caramia, 1966a). Previous studies showed a prominent role for testosterone in the maintenance of the GCTs (Berkman and Kronman, 1970). For example, castrated male mice have regressed GCTs that resemble those of female mice (Bhoola et al., 1973; Caramia, 1966a, b; Chretien, 1977; Kaiho et al., 1975; Rogers and Brown-Grant, 1971). Moreover, mice with testicular feminization (*Tfm*), a spontaneous single-base deletion in the androgen receptor (*Ar*) gene, have GCTs with fewer secretory granules and increased cytoplasmic vacuoles (Matsuura et al., 1984). A recent study shows that mice deficient for *Ar* (*Ar^{F/F};CAG-Cre* mice) exhibit GCT maturation defects (Adthapanyawanich et al., 2015). Thus, GCT maturation in the SMGs in male mice is one of the established models to study androgen-dependent non-gonadal tissue differentiation.

Autophagy—Greek for "the eating of oneself"—is a major catabolic process that degrades cytoplasmic components and proteins via the ubiquitin-proteasome system (Shintani and Klionsky, 2004). A growing numbers of studies indicate that autophagy and autophagy-related molecules play a crucial role in cell differentiation (Mizushima and Levine, 2010). In addition, a relationship between cholesterol metabolism and autophagy regulation has been suggested in several pathological conditions (Barbero-Camps et al., 2018; Cheng et al., 2006; Seo et al., 2011); however, the nature of this relationship has not been clarified yet in development and organogenesis.

In this study, we show that excessive cholesterol synthesis in the salivary glands results in differentiation defects in the duct system, through the inactivation of autophagy, in mice with an epithelial tissue-specific deletion of either *Insig1/2*, an endogenous inhibitor for an HMG-CoA reductase that enhances cholesterol synthesis, or *Atg7*, a key enzyme for autophagy.

RESULTS

Male mice with excessive cellular cholesterol synthesis display maturation defects in the granular convoluted tubules of the submandibular glands

To investigate the contribution of cellular cholesterol metabolism to salivary gland development, we analyzed mice with an epithelial tissue-specific deletion of the *Insig1* and *Insig2* genes (*K14-Cre;Insig1$^{F/F}$;Insig2$^{-/-}$* mice, hereafter *Insig1/2* cKO mice). To investigate the early developmental stage of salivary duct formation, we conducted histological analysis of the SMGs in male and female wild-type (WT) and *Insig1/2* cKO mice at E14.5, and from P0 to P21, and detected no developmental defects in both sexes until P21 (Fig. S1). However, male *Insig1/2* cKO mice exhibited impaired GCT formation. GCTs differentiated from SDs after postnatal day (P) 28 when the male mice reached sexual maturity (Fig. 1A). The ductal area in the submandibular glands was significantly reduced from 48% and 53% to 15% and 30% at P28 and P56, respectively, in male *Insig1/2* cKO mice without altered cell proliferation and death (Fig. 1B; Fig. S2). Consistent with the GCT maturation defects in *Insig1/2* cKO mice, there were a few eosinophilic granules in the apical cytoplasm of GCT cells, while GCTs in WT control mice contained abundant granules (Fig. 1C). We confirmed that loss of *Insig1/2* had less impact on other cell types (Fig. S3).

Compromised androgen receptor signaling in the granular convoluted tubules in *Insig1/2* cKO mice

To examine the androgen receptor (AR) signaling pathway, we performed quantitative RT-PCR analyses for the cysteine-rich secretory protein 3 (*Crisp3*), epidermal growth factor (*Egf*), and nerve growth factor (*Ngf*), which are known as downstream targets of the AR pathway (Schwidetzky et al., 1995), in the SMGs of WT control and *Insig1/2* cKO mice. We confirmed that development of the testes, the main source of androgens, was not affected in *Insig1/2* cKO mice (Fig. 1D, E; Fig. S3E). While *Ar* expression was not altered in the SMGs of *Insig1/2* cKO mice, compared to that of WT control mice, expression of *Crisp3*, *Egf* and *Ngf* was significantly downregulated in P28 and P56 SMGs of *Insig1/2* cKO mice (Fig. 1F; Fig. S4). The GCTs contain numerous secretory granules that contain EGF and NGF in the cytosol on the apical side of the nucleus (Barka, 1980; Gresik et al., 1981; Mudd and White, 1975). As expected, we detected EGF- and NGF-positive GCT cells in the SMGs of WT mice. By contrast, these cells were dramatically decreased in number in *Insig1/2* cKO mice (Fig. 1G, H; Fig. S4, S5). Taken together, our results indicate that excessive cholesterol synthesis results in impaired GCT maturation in *Insig1/2* cKO mice.

Increased Cholesterol Synthesis Suppresses *Atg7* Expression

Several studies suggest that cholesterol metabolism may be linked to the regulation of autophagy and/or of the autophagic machinery (Cheng et al., 2006; Seo et al., 2011). In addition, increasing numbers of studies indicate that molecules involved in autophagy play crucial roles in a variety of non-autophagy pathways, including differentiation (Subramani and Malhotra, 2013). To investigate the link between aberrant cholesterol metabolism and autophagy activity, we

performed immunohistochemical analyses for LC3, ubiquitin (Ub), and p62/SQSTM1, an adaptor/receptor protein for ubiquitinated proteins (Komatsu et al., 2007), in the SMGs of *Insig1/2* cKO and WT mice. Previous studies show that Ub and p62/SQSTM1 increase when autophagy is suppressed (Ichimura et al., 2008; Komatsu et al., 2005). We found that Ub and p62/SQSTM1 accumulated only in SMG duct cells of *Insig1/2* cKO mice (Fig. 2A). We further confirmed these findings by immunoblotting (Fig. 2B). In addition, we treated SMG explants from P28 male WT and *Insig1/2* cKO mice with rapamycin, an autophagy inducer, or bafilomycin, an autophagy inhibitor that blocks fusion of autophagosomes with the lysosomes, in order to investigate the flux of autophagy (Klionsky et al., 2016) (Fig. 2C). We found that the steady state level of autophagy was decreased due to decreased autophagic flux in the SMGs of *Insig1/2* cKO mice compared to WT controls (Fig. 2D). Taken together, our results strongly suggest that autophagy is compromised in *Insig1/2* cKO mice, resulting in a failure of GCT to differentiate in the SMGs. To investigate whether and how the autophagic machinery was involved in the altered GCT differentiation in the SMGs of *Insig1/2* cKO mice, we performed PCR array analyses for molecules related to the autophagic machinery (*Atg3*, *Atg5*, *Atg7*, *Atg10*, *Atg12*, and *Beclin1*). Among them, expression of *Atg7*, a key enzyme for autophagy and autophagic machinery, was specifically and significantly decreased (Fig. 2E). Previous studies indicate that *Insig1/2* deficiency results in increased translocation of the sterol regulatory element-binding protein (SREBP) to the nucleus (Engelking et al., 2005). As expected, SREBP1 and SREBP2 protein levels were increased in the nucleus in *Insig1/2* cKO SMGs compared to controls, suggesting that these increased SREBPs suppressed *Atg7* expression (Fig. 2F). Bioinformatics analyses revealed that there was a putative sterol regulatory element (SRE; 5'-CTGGGGTGT-3'), where SREBP can bind, in the *Atg7* promotor region (-384bp to -376bp). To test the binding of SREBP proteins (SREBP1 and SREBP2) to the

Agt7 promoter region, we performed chromatin immunoprecipitation (ChIP) assays and found that both SREBP1 and SREBP2 could bind to the *Atg7* promoter region in WT SMGs, but not in *Insig1/2* cKO SMGs (Fig. 2G). Thus, while SREBP levels increased in the nucleus of the cells in SMGs of *Insig1/2* cKO mice, these SREBPs failed to bind the *Atg7* promoter region in the *Insig1/2* cKO background. The epigenetic mechanism involved in the regulation of *Atg7* promoter accessibility is currently unknown and likely complex.

Male mice deficient for *Atg7* display similar maturation defects in the granular convoluted tubules of the submandibular glands

To confirm that autophagy deficiency results in GCT maturation defects, we analyzed mice deficient for *Atg7*, a key enzyme for autophagy, in the salivary glands ($Atg7^{F/F}$;*K14-Cre* mice; hereafter *Atg7* cKO mice). As expected, male *Atg7* cKO mice exhibited GCT maturation defects, as seen in *Insig1/2* cKO mice. GCT differentiation was remarkably suppressed in the SMGs of *Atg7* cKO mice at P28 and at a later age, while there was no duct developmental defect before P21 (Fig. 3A, B; Fig. S6-9). The ductal area was significantly decreased in the SMGs of P56 *Atg7* cKO mice, compared to those of WT control mice (Fig. 3C). There was less impact on duct formation in female P56 *Atg7* cKO mice (Fig. S10, S11). Without defects in testis development (Fig. 3D, E; Fig. S8F), the expression of molecules regulated through the AR signaling pathway was significantly downregulated in the SMGs of male *Atg7* cKO mice, as seen in *Insig1/2* cKO mice (Fig. 3F–H; Fig. S9). The autophagy deficiency in *Atg7* cKO mice was confirmed with immunohistochemical staining and immunoblotting for Ub and p62 (Fig. S12).

Autophagy regulates granular convoluted tubule differentiation through NRF2-mediated *Foxa1* expression

Previous studies indicate that the cytosolic accumulation of p62/SQSTM1 consequently results in the activation of the NRF2 cascade (Ichimura and Komatsu, 2018). To evaluate NRF2 activation/ translocation to the nuclei, we carried out immunohistochemical staining of NRF2 in the SMGs of *Insig1/2* cKO and *Atg7* cKO mice. We found that NRF2 was accumulated in the nuclei of duct cells in *Insig1/2* cKO and *Atg7* cKO mice, but not in WT control mice (Fig. 4A). *Ar* expression was not altered in either *Insig1/2* cKO or *Atg7* cKO mice, compared to WT control mice (Fig. 1F, 3F; Fig. S4D, S9A). The gene expression of AR downstream targets is regulated through a complex of Forkhead box protein A1 (FOXA1) and AR (Augello et al., 2011). *Foxa1* expression was decreased in the SMGs of *Insig1/2* cKO and *Atg7* cKO mice, compared to WT controls, at P56 (Fig. 4B). Moreover, gene expression related to endoplasmic reticulum (ER) stress was not altered in the SMGs of *Insig1/2* cKO and *Atg7* cKO mice, compared to WT controls (Fig. S13). We therefore hypothesized that the accumulated NRF2 suppressed *Foxa1* expression, but not directly *Ar* expression. To examine whether and how NRF2 regulates *Foxa1* expression, we performed a bioinformatics analysis for the *Foxa1* promoter region and found that it contains four putative NRF2-binding sites [*aka* the antioxidant response element (ARE)] (Fig. 4C; Fig. S14). To validate the binding of NRF2 to the *Foxa1* promoter region, we conducted ChIP assays and found that NRF2 bound to the NRF2-binding sites (BSs)-3/4, but not to the NRF2 BSs-1/2, in the *Foxa1* promotor region (Fig. 4D). Furthermore, we confirmed that FOXA1 expression was decreased in the SMGs of *Insig1/2* cKO and *Atg7* cKO mice (Fig. 4E). Taken together, our results indicate that impaired autophagy results in GCT maturation defects through the NRF2–FOXA1 mechanism (Fig. S15).

DISCUSSION

NRF2 was originally proposed to be a cytoprotective factor against reactive oxygen species, as well as chemical, electrophile, and oxidative stresses. Under normal conditions, NRF2 binds kelch-like ECH-associated protein1 (KEAP1), a sole ubiquitin ligase adaptor protein for NRF2, and is degraded by the ubiquitin-proteasome pathway. In presence of a cellular stress, KEAP1 is inactivated so that NRF2 is stabilized and translocates into the nucleus, where it induces the expression of genes involved in cytoprotective roles (*aka* canonical KEAP1-NRF2 pathway). On the other hand, p62 interacts with KEAP1 at the NRF2-binding site, which inhibits binding of KEAP1 to NRF2 in the noncanonical KEAP1-NRF2 pathway. This interaction leads to the release of NRF2 from a degradation complex; the stabilized NRF2 then translocates into the nucleus to regulate target gene expression (Jain et al., 2010). The noncanonical KEAP1-NRF2 pathway has been suggested to have a role in development, disease, and specifically cancer. For example, a deficiency of *Atg7* in paired box 7 (Pax7)-positive muscle satellite cells (*Atg7^{F/F};Pax7-Cre* mice) results in dwarfism and decreased skeletal muscle mass in male mice only after P14, which are due to cell proliferation defects through decreased NRF2-target gene expression in the satellite cells (Zecchini et al., 2018). In this study, we found that an activated noncanonical KEAP1-NRF2 pathway resulted in a maturation defect of the GCTs in the SMGs of *Insig1/2* cKO and *Atg7* cKO mice through suppressed *Foxa1* expression. GCT differentiation is distinct after the onset of puberty in male rodents. Therefore, the GCT in the SMGs is a suitable model tissue to study how sex hormones contribute to non-gonadal organ development. The mechanism revealed in this study may be conserved in the development of various non-gonadal organs with a variety of degrees, since sex hormone receptors are differently expressed in each tissue and cell type.

Salivary gland cancers occur with a prevalence of 6% among head and neck cancers in the United States. Although there is no salivary duct carcinoma in *Insig1/2* cKO and *Atg7* cKO mice, these mice may have a higher probability of developing cancer when exposed to some carcinogens. Expression of AR in the salivary glands of these patients varies by tumor type and accounts for 0 to 86 % of cases (Dalin et al., 2017). Among them, salivary duct carcinoma is the most frequent AR-expressing cancer, ranging from 64 to 98 % of the cases. Excessive activation of AR signaling is strongly associated with the prognosis and malignancy of cancers in the salivary glands, prostate, and breast (Dai et al., 2017; Giovannelli et al., 2018; Robinson et al., 2015). Interestingly, several studies indicate that expression of *NRF2* and *NRF1* is associated with prostate cancers via AR transactivation in humans and mice (Frohlich et al., 2008; Schultz et al., 2014). Indeed, NRF2 activation with either bardoxolone, sulforaphane, or curcumin suppresses AR signaling in prostate cancer cell lines (Khurana and Sikka, 2018). Thus, impaired autophagy accelerates NRF2 accumulation, which suppresses AR signaling not only during GCT maturation but also in cancers.

In addition to FOXA1 binding directly to the consensus sequence (the FKHD motif) to regulate target gene expression, FOXA1 opens chromatin and recruits other transcription factors, such as AR and estrogen receptor alpha (ERα), to their binding sites in the target genes (Jin et al., 2014). *Foxa1* null (*Foxa1$^{-/-}$*) mice die within 2 weeks after birth and display impaired differentiation of secretory luminal epithelial cells and dysregulated ductal pattern in the prostate (Gao et al., 2005). FOXA1 also plays important roles in bile duct differentiation (Li et al., 2009). Mice with a tissue-specific deficiency for *Foxa1* in the mammary glands or epithelial cells (*Foxa1$^{F/F}$;MMTC-Cre* and *Foxa1$^{F/F}$;K14-Cre* mice, respectively) exhibit impaired differentiation of the mammary gland ducts through decreased ERα expression, while the alveolar-lineage cells develop and differentiate normally (Bernardo et al., 2010). Thus, *Foxa1* is a promising target gene

of the AR signaling in duct development. Mutations in the *FOXA1* gene are also associated with the prognosis of human salivary duct carcinoma (Urano et al., 2018), breast cancer (Rangel et al., 2018; Robinson and Carroll, 2012), and prostate cancer (Robinson and Carroll, 2012).

In summary, we found that, in *Insig1/2* and *Atg7* cKO mice, *Foxa1* expression was compromised through the ATG7-mediated NRF2 pathway, which in turn resulted in the suppression of AR signaling during duct formation, without developmental defects in acinar cells. This mechanism may be applicable to the development of other ductal and non-gonadal organs.

MATERIALS AND METHODS

Animals

Insig1$^{F/F}$;Insig2$^{-/-}$ (Engelking et al., 2005) and *K14-Cre* (Dassule et al., 2000) mice were obtained from The Jackson Laboratory. *Atg7$^{F/F}$* mice (Komatsu et al., 2005) were a gift from Dr. Masaaki Komatsu (Juntendo University, Tokyo, Japan). *Insig1$^{F/F}$;Insig2$^{-/-}$* and *Atg7$^{F/F}$* mice were crossed with *K14-Cre* mice to generate *Insig1/2* cKO and *Atg7* cKO mice, respectively. Genotyping was performed using PCR primers, as previously described (Dassule et al., 2000; Engelking et al., 2005; Komatsu et al., 2005).

Histology

Hematoxylin Eosin (H&E) staining, Chromotrope-Aniline blue (CAB) staining, and immunohistochemistry were performed as previously described (Suzuki et al., 2018). The antibodies used for immunohistochemistry were rabbit polyclonal antibodies against EGF (Abcam), LC3 (Cell Signaling Technology), NGF (Abcam), ubiquitin (DAKO), α-SMA (Abcam), AQP5 (Alomone labs), and LAMP2 (Abcam), rabbit monoclonal antibodies against AR (Abcam),

NRF2 (Abcam), c-KIT (Cell Signaling Technology), Ki67 (Abcam), KRT17/19 (Cell Signaling Technology), and MIST1 (Cell Signaling Technology), and a mouse monoclonal antibody against p62/SQSTM1 (Abcam) (Supplementary Table S1). Fluorescence images were obtained using a confocal microscope (Ti-C2, Nikon). Color images were obtained using a light microscope (BX43, Olympus) (n=6 per group). TUNEL staining was performed using a Click-iT® Plus TUNEL Assay kit with Alexa 594 (C10618, Molecular probes), according to the manufacturer's instructions. Fat deposits were investigated by Oil Red O staining. Briefly, frozen sections were fixed in 4% paraformaldehyde (PFA), washed with distilled water, rinsed with 60% isopropanol, stained with Oil Red O (0.18% w/v in isopropanol) for 15 min, and then rinsed with 60% isopropanol and counterstained with 0.04% methylene blue for the nuclei. For Nile Red staining, a stock solution of Nile Red (500 µg/ml) in acetone was prepared and stored chilled and protected from light. A fresh staining solution of Nile Red was made by adding 2-10 µl of the stock solution to 1 mL of 75% glycerol, followed by brisk vortexing. To stain frozen tissue sections, a drop of the glycerol staining solution was added to each section. After 5 min, the sections were examined under the fluorescence microscope (Nikon, ECLIPSE Ti). For Periodic acid-Schiff (PAS) staining, the slides were rehydrated and quenched in 0.5% periodic acid solution for 5 min, followed by 15 min in Schiff's reagent.

Organ cultures

SMG explants were dissected out from P28 mice and sliced with 1 mm of thickness and then incubated in BGjB medium (Gibco) supplemented with 10% fetal bovine serum (FBS), 0.1 mg/mL ascorbic acid, and penicillin/streptomycin, in a rotor incubator at 37°C for 24 hours. The SMG

explants were treated with or without rapamycin (LC Laboratories; 200 nM) and bafilomycin (Sigma; 100 nM) for 24 hours.

Immunoblotting

SMG tissues were lysed in T-PER^{TM} Tissue Protein Extraction Reagent (Thermo Scientific). Cell fractionation was performed using a NE-PER^{TM} nuclear and cytoplasmic extraction kit (Thermo Scientific). Equal amounts of protein were analyzed by SDS- PAGE, followed by electrophoretic transfer to PVDF membranes (Millipore Corp., Billerica, MA, USA). The membrane was blocked for 1 hour with blocking buffer (5% skim milk in TBS) and incubated overnight at 4°C with a primary antibody. The antibodies used for immunoblotting were as follows: anti-INSIG1 rabbit polyclonal (Abcam), anti-INSIG2 rabbit polyclonal (Abcam), anti-HMGCR rabbit polyclonal (Santa Cruz), anti-ubiquitin rabbit polyclonal (Dako), anti-p62 mouse monoclonal (Abcam), anti-LC3 rabbit polyclonal (Cell Signaling Technology), anti-ATG7 rabbit polyclonal (Cell Signaling Technology), anti-SREBP1 mouse monoclonal (Novus Biologicals), anti-SREBP2 rabbit polyclonal (Novus Biologicals), anti-histone H3 rabbit polyclonal (Cell Signaling Technology), and anti-GAPDH mouse monoclonal (Millipore) (Supplementary Table S1).

Quantitative RT-PCR

Total RNAs isolated from the submandibular salivary glands (n=6 per group) were dissected with the QIAshredder and RNeasy mini extraction kit (QIAGEN), as previously described (Suzuki et al., 2015). *Gapdh* was used as an internal housekeeping control. The ΔΔ-CT method was applied for the analyses. The following PCR primers were used for further specific analysis: *Atg3*, 5'-CATGCAGGCATGCTGAAGTGATG-3' and 5'-TCGTCTGACAGGGGAAACCC-3'; *Atg5*, 5'-

ACCTCGGTTTGGCTTTGGTT-3' and 5'-TCAGGGGTGTGCCTTCATATTC-3'; *Atg7*, 5'-ATGCCAGGACACCCTGTGAACTTC-3' and 5'-ACATCATTGCAGAAGTAGCAGCCA-3'; *Atg10*, 5'-CGAGCGAGCGGGTTCTCATT-3' and 5'-CCAGAGCTAACGGTCTCCCA-3'; *Atg12*, 5'-TGCTGAAGGCTGTAGGAGAC-3' and 5'-TTACCATCACTGCCAAAACACTCA-3'; *Beclin1*, 5'-ACTCACAGCTCCATTACTTACCAC-3' and 5'-CTGTGCATTCCTCACACAGC-3'; *Ar*, 5'-TCTGCCTCCGAAGTGTGGTA-3' and 5'-ACTTCTGTTTCCCTTCAGCGG-3'; *Crisp3*, 5'-ACAGTGGCCATTATCCAAGCA-3' and 5'-GCATGTAGCTAGGCAACGTTTT-3'; *Egf*, 5'-TAAGGATCCTGACCCCGAACTT-3' and 5'-CAAATCCTGTGGGGCATGTG-3'; *Ngf*, 5'-GGAGCGCATCGAGTGACTT-3' and 5'-CCTCACTGCGGCCAGTATAG-3'; *Foxa1*, 5'-GACGCCAAGACATTCAAGCG-3' and 5'-ATCGTGCCACCTTGACGAAA-3'; *Fas*, 5'-GACCTCAGGCTGCAGTGAAT-3' and 5'-GTCCCACTTGATGTGAGGGG-3'; *Scd1*, 5'-GAGTAGCTGAGCTTTGGGCT-3' and 5'-ACTTCATCAGCGGGGACTTG-3'; *Foxo1*, 5'-TGTACAGCGCATAGCACCAA-3' and 5'-CCGATGGACGGAATGAGAGG-3'; *Foxo3*, 5'-GAGCTGGAGCTCGAACCTT-3' and 5'-TGTGCCGGATGGAGTTCTTC-3'; *Chop*, 5'-CCTGGTATGAGGATCTGCAG-3' and 5'-GTTTCCTAGTTCTTCCTTGCTCTTC-3'; *Ire1a*, 5'-CACTGCCTGAGACCTTGTTG-3' and 5'-TGTTGGGACCTGCAGGAC-3'; *β-actin*, 5'-ACAATGAGCTGCGTGTGG-3' and 5'-GACAGCACAGCCTGGATG-3' and *Gapdh*, 5'-AACTTTGGCATTTGGAAGG-3' and 5'-ACACATTGGGGGTAGGAACA-3'.

Comparative analysis of transcription factor binding sites

The UCSC genome browser was used to obtain the genomic sequences of the murine *Ar* gene (NC_000086.7), *Atg7* gene (NC_000072.6) and *Foxa1* gene (NC_000078.6), including the 5-kbp

sequence upstream of the respective transcription start site. The sequence was then mapped to seven additional mammalian genomes [human (Build 38), chimpanzee (Build 2.1.4), orangutan (Build 2.0.2), rhesus macaque (Build 1.0), rat (Build 5), dog (Build 3.1), and horse (Build equCab2)] with the BLAST tool, as previously described (Suzuki et al., 2015). The multiple alignments were obtained using the Clustal Omega tool with default parameters and settings (Sievers et al., 2011). The antioxidant response element (ARE), which resembles the NRF2 binding motif (5'-TGAG/CNNNGC-3'), and the sterol response element (SRE), which resembles the sterol regulatory element-binding protein (SREBP) binding sites (5'-TCACNCCAC-3'), were searched in the aligned DNA sequences.

ChIP assay

Tissue extracts from the salivary glands were incubated with either rabbit polyclonal NRF2 antibody (Abcam), normal rabbit IgG (Santa Cruz Biotechnology), mouse monoclonal SREBP1 antibody (Santa Cruz Biotechnology), mouse monoclonal SREBP2 antibody (Santa Cruz Biotechnology) or normal mouse IgG (Santa Cruz Biotechnology) overnight at 4°C, followed by precipitation with magnetic beads. Washing and elution of the immune complexes, as well as DNA precipitation, were performed according to standard procedures, as previously described (Suzuki et al., 2015). The putative ARE on the *Foxa1* promoter in the immune complexes was detected by PCR using the following primers: for sites 1 and 2, 5'- *CCAGGTCGGCCTAACGTC*-3' (−1002 bp to −985 bp) and 5'-*ACTACCCCTACTTCCCGGC*-3' (−904 bp to −886 bp); for sites 3 and 4, 5'-*ATCCGCCTGCCTTATCACAC*-3' (−1201 bp to −1182 bp) and 5'-*GAAACTCGTACCTGCGGCT*-3' (−1053 bp to −935 bp). The putative SRE on the *Atg7* gene in the immune complexes was detected by PCR using the following primers: 5'-TCCCAGGCCAAGGATACATG-3' (-641 bp

to -622 bp) and 5'-AGTCTCTTAGCTATCCAGGCA-3' (−356 bp to −336 bp). The positions of the PCR fragments correspond to NCBI mouse genome Build 38 (mm10).

Statistics

The two-tailed student's *t* test was applied for statistical analysis. A *p* value < 0.05 was considered statistically significant. For all graphs, data are represented as mean ± standard deviation.

References

Adthapanyawanich, K., Kumchantuek, T., Nakata, H., Yamamoto, M., Wakayama, T., Nishiuchi, T., and Iseki, S. (2015). Morphology and gene expression profile of the submandibular gland of androgen-receptor-deficient mice. Archives of oral biology *60*, 320-332.

Augello, M.A., Hickey, T.E., and Knudsen, K.E. (2011). FOXA1: master of steroid receptor function in cancer. EMBO J *30*, 3885-3894.

Barbero-Camps, E., Roca-Agujetas, V., Bartolessis, I., de Dios, C., Fernandez-Checa, J.C., Mari, M., Morales, A., Hartmann, T., and Colell, A. (2018). Cholesterol impairs autophagy-mediated clearance of amyloid beta while promoting its secretion. Autophagy *14*, 1129-1154.

Barka, T. (1980). Biologically active polypeptides in submandibular glands. The journal of histochemistry and cytochemistry : official journal of the Histochemistry Society *28*, 836-859.

Berkman, M.D., and Kronman, J.H. (1970). A histochemical study of the effects of castration and testosterone administration on the major salivary glands of Swiss mice. Acta anatomica *76*, 200-219.

Bernardo, G.M., Lozada, K.L., Miedler, J.D., Harburg, G., Hewitt, S.C., Mosley, J.D., Godwin, A.K., Korach, K.S., Visvader, J.E., Kaestner, K.H., et al. (2010). FOXA1 is an essential determinant of ERalpha expression and mammary ductal morphogenesis. Development *137*, 2045-2054.

Bhoola, K.D., Dorey, G., and Jones, C.W. (1973). The influence of androgens on enzymes (chymotrypsin-and trypsin-like proteases, renin, kallikrein and amylase) and on cellular structure of the mouse submaxillary gland. J Physiol *235*, 503-522.

Caramia, F. (1966a). Ultrastructure of mouse submaxillary gland. I. Sexual differences. Journal of ultrastructure research *16*, 505-523.

Caramia, F. (1966b). Ultrastructure of mouse submaxillary gland. II. Effect of castration in the male. Journal of ultrastructure research *16*, 524-536.

Cheng, J., Ohsaki, Y., Tauchi-Sato, K., Fujita, A., and Fujimoto, T. (2006). Cholesterol depletion induces autophagy. Biochemical and biophysical research communications *351*, 246-252.

Chretien, M. (1977). Action of testosterone on the differentiation and secretory activity of a target organ: the submaxillary gland of the mouse. International review of cytology *50*, 333-396.

Dai, C., Heemers, H., and Sharifi, N. (2017). Androgen Signaling in Prostate Cancer. Cold Spring Harbor perspectives in medicine *7*.

Dalin, M.G., Watson, P.A., Ho, A.L., and Morris, L.G. (2017). Androgen Receptor Signaling in Salivary Gland Cancer. Cancers *9*.

Dassule, H.R., Lewis, P., Bei, M., Maas, R., and McMahon, A.P. (2000). Sonic hedgehog regulates growth and morphogenesis of the tooth. Development *127*, 4775-4785.

Dunn, J.F., and Wilson, J.D. (1975). Developmental study of androgen responsiveness in the submandibular gland of the mouse. Endocrinology *96*, 1571-1578.

Engelking, L.J., Liang, G., Hammer, R.E., Takaishi, K., Kuriyama, H., Evers, B.M., Li, W.P., Horton, J.D., Goldstein, J.L., and Brown, M.S. (2005). Schoenheimer effect explained-- feedback regulation of cholesterol synthesis in mice mediated by Insig proteins. The Journal of clinical investigation *115*, 2489-2498.

Frohlich, D.A., McCabe, M.T., Arnold, R.S., and Day, M.L. (2008). The role of Nrf2 in increased reactive oxygen species and DNA damage in prostate tumorigenesis. Oncogene *27*, 4353-4362.

Gao, N., Ishii, K., Mirosevich, J., Kuwajima, S., Oppenheimer, S.R., Roberts, R.L., Jiang, M., Yu, X., Shappell, S.B., Caprioli, R.M., et al. (2005). Forkhead box A1 regulates prostate ductal morphogenesis and promotes epithelial cell maturation. Development *132*, 3431-3443.

Giovannelli, P., Di Donato, M., Galasso, G., Di Zazzo, E., Bilancio, A., and Migliaccio, A. (2018). The Androgen Receptor in Breast Cancer. Frontiers in endocrinology *9*, 492.

Gresik, E.W., Schenkein, I., van der Noen, H., and Barka, T. (1981). Hormonal regulation of epidermal growth factor and protease in the submandibular gland of the adult mouse. Endocrinology *109*, 924-929.

Ichimura, Y., and Komatsu, M. (2018). Activation of p62/SQSTM1-Keap1-Nuclear Factor Erythroid 2-Related Factor 2 Pathway in Cancer. Frontiers in oncology *8*, 210.

Ichimura, Y., Kominami, E., Tanaka, K., and Komatsu, M. (2008). Selective turnover of p62/A170/SQSTM1 by autophagy. Autophagy *4*, 1063-1066.

Jain, A., Lamark, T., Sjottem, E., Larsen, K.B., Awuh, J.A., Overvatn, A., McMahon, M., Hayes, J.D., and Johansen, T. (2010). p62/SQSTM1 is a target gene for transcription factor NRF2 and creates a positive feedback loop by inducing antioxidant response element-driven gene transcription. The Journal of biological chemistry *285*, 22576-22591.

Jin, H.J., Zhao, J.C., Wu, L., Kim, J., and Yu, J. (2014). Cooperativity and equilibrium with FOXA1 define the androgen receptor transcriptional program. Nature communications *5*, 3972.

Kaiho, M., Nakamura, T., and Kumegawa, M. (1975). Morphological studies on the synthesis of secretory granules in convoluted tubules of mouse submandibular gland. The Anatomical record *183*, 405-419.

Khurana, N., and Sikka, S.C. (2018). Targeting Crosstalk between Nrf-2, NF-kappaB and Androgen Receptor Signaling in Prostate Cancer. Cancers *10*.

Klionsky, D.J., Abdelmohsen, K., Abe, A., Abedin, M.J., Abeliovich, H., Acevedo Arozena, A., Adachi, H., Adams, C.M., Adams, P.D., Adeli, K., et al. (2016). Guidelines for the use and interpretation of assays for monitoring autophagy (3rd edition). Autophagy *12*, 1-222.

Komatsu, M., Waguri, S., Koike, M., Sou, Y.S., Ueno, T., Hara, T., Mizushima, N., Iwata, J., Ezaki, J., Murata, S., et al. (2007). Homeostatic levels of p62 control cytoplasmic inclusion body formation in autophagy-deficient mice. Cell *131*, 1149-1163.

Komatsu, M., Waguri, S., Ueno, T., Iwata, J., Murata, S., Tanida, I., Ezaki, J., Mizushima, N., Ohsumi, Y., Uchiyama, Y., et al. (2005). Impairment of starvation-induced and constitutive autophagy in Atg7-deficient mice. The Journal of cell biology *169*, 425-434.

Li, Z., White, P., Tuteja, G., Rubins, N., Sackett, S., and Kaestner, K.H. (2009). Foxa1 and Foxa2 regulate bile duct development in mice. The Journal of clinical investigation *119*, 1537-1545.

Matsuura, S., Sahara, N., and Suzuki, K. (1984). Fine structure of submandibular glands of mice with testicular feminization (Tfm/Y). Cell and tissue research *235*, 295-301.

Mizushima, N., and Levine, B. (2010). Autophagy in mammalian development and differentiation. Nature cell biology *12*, 823-830.

Mudd, B.D., and White, S.C. (1975). Sexual dimorphism in the rat submandibular gland. Journal of dental research *54*, 193.

Pinkstaff, C.A. (1980). The cytology of salivary glands. International review of cytology *63*, 141-261.

Rangel, N., Fortunati, N., Osella-Abate, S., Annaratone, L., Isella, C., Catalano, M.G., Rinella, L., Metovic, J., Boldorini, R., Balmativola, D., et al. (2018). FOXA1 and AR in invasive breast cancer: new findings on their co-expression and impact on prognosis in ER-positive patients. BMC cancer *18*, 703.

Robinson, D., Van Allen, E.M., Wu, Y.M., Schultz, N., Lonigro, R.J., Mosquera, J.M., Montgomery, B., Taplin, M.E., Pritchard, C.C., Attard, G., et al. (2015). Integrative Clinical Genomics of Advanced Prostate Cancer. Cell *162*, 454.

Robinson, J.L., and Carroll, J.S. (2012). FoxA1 is a key mediator of hormonal response in breast and prostate cancer. Frontiers in endocrinology *3*, 68.

Rogers, A.W., and Brown-Grant, K. (1971). The effects of castration on the ultrastructure and the iodide-concentrating ability of mouse submaxillary salivary glands. Journal of anatomy *109*, 51-62.

Schultz, M.A., Hagan, S.S., Datta, A., Zhang, Y., Freeman, M.L., Sikka, S.C., Abdel-Mageed, A.B., and Mondal, D. (2014). Nrf1 and Nrf2 transcription factors regulate androgen receptor transactivation in prostate cancer cells. PloS one *9*, e87204.

Schwidetzky, U., Haendler, B., and Schleuning, W.D. (1995). Isolation and characterization of the androgen-dependent mouse cysteine-rich secretory protein-3 (CRISP-3) gene. The Biochemical journal *309 (Pt 3)*, 831-836.

Seo, Y.K., Jeon, T.I., Chong, H.K., Biesinger, J., Xie, X., and Osborne, T.F. (2011). Genome-wide localization of SREBP-2 in hepatic chromatin predicts a role in autophagy. Cell metabolism *13*, 367-375.

Shintani, T., and Klionsky, D.J. (2004). Autophagy in health and disease: a double-edged sword. Science *306*, 990-995.

Sievers, F., Wilm, A., Dineen, D., Gibson, T.J., Karplus, K., Li, W., Lopez, R., McWilliam, H., Remmert, M., Soding, J., et al. (2011). Fast, scalable generation of high-quality protein multiple sequence alignments using Clustal Omega. Mol Syst Biol *7*, 539.

Subramani, S., and Malhotra, V. (2013). Non-autophagic roles of autophagy-related proteins. EMBO reports *14*, 143-151.

Suzuki, A., Minamide, R., and Iwata, J. (2018). WNT/beta-catenin signaling plays a crucial role in myoblast fusion through regulation of Nephrin expression during development. Development.

Suzuki, A., Pelikan, R.C., and Iwata, J. (2015). WNT/beta-Catenin Signaling Regulates Multiple Steps of Myogenesis by Regulating Step-Specific Targets. Molecular and cellular biology *35*, 1763-1776.

Urano, M., Hirai, H., Tada, Y., Kawakita, D., Shimura, T., Tsukahara, K., Kano, S., Ozawa, H., Okami, K., Sato, Y., et al. (2018). The high expression of FOXA1 is correlated with a favourable prognosis in salivary duct carcinomas: a study of 142 cases. Histopathology *73*, 943-952.

Zecchini, S., Giovarelli, M., Perrotta, C., Morisi, F., Touvier, T., Di Renzo, I., Moscheni, C., Bassi, M.T., Cervia, D., Sandri, M., et al. (2018). Autophagy controls neonatal myogenesis by regulating the GH-IGF1 system through a NFE2L2- and DDIT3-mediated mechanism. Autophagy, 1-20.
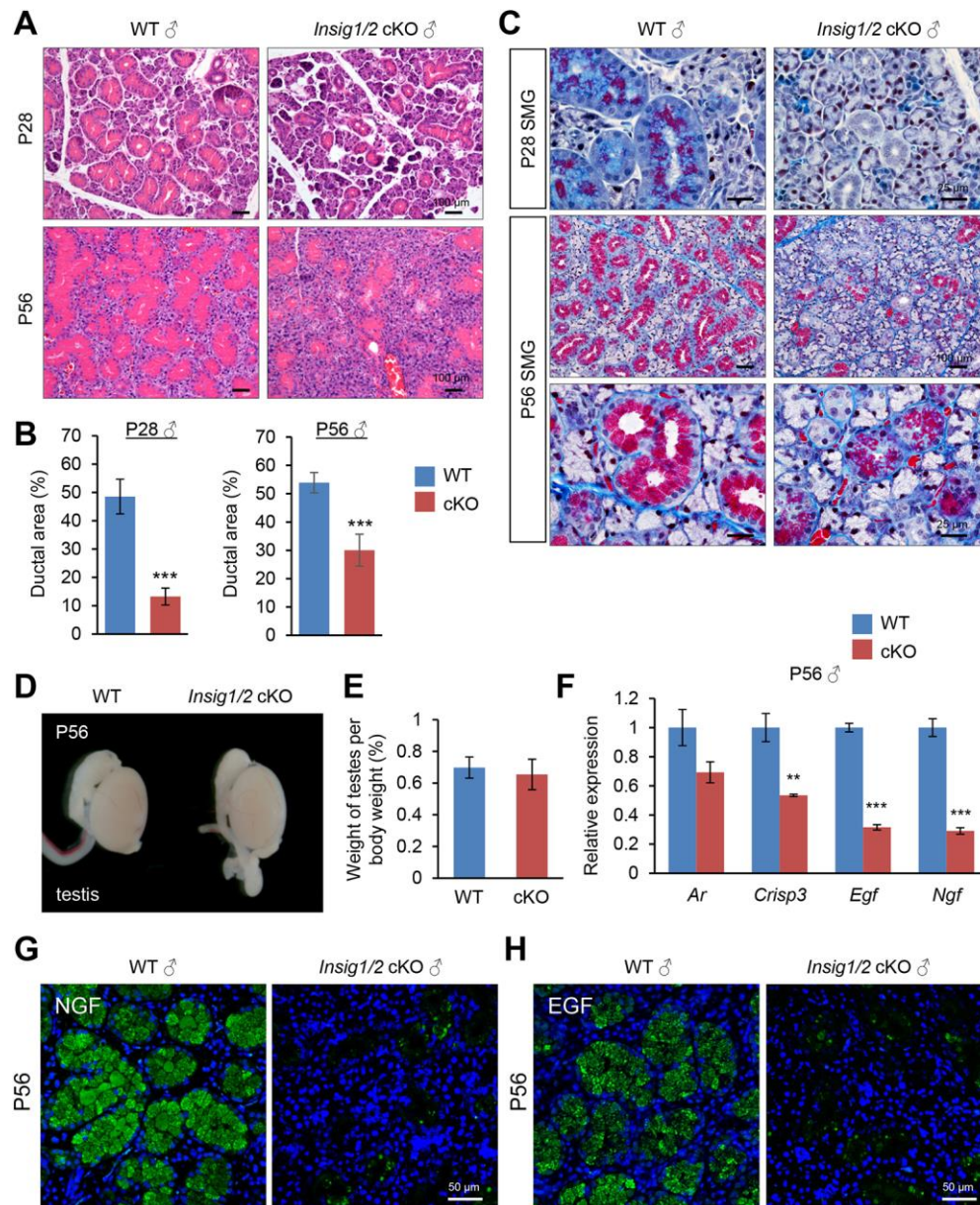
Figures

Fig. 1. Phenotypic analyses of the salivary glands of *Insig1^{F/F};Insig2^{-/-};K14-Cre* cKO mice.

(A) H&E staining of the submandibular glands (SMGs) from P28 and P56 male wild-type (WT)

control and *Insig1/2* cKO mice. Scale bars; 100 μm. (B) Quantification of ductal area per total

gland area in P28 and P56 male WT (blue bars) and *Insig1/2* cKO (red bars) SMGs. n=6 per group. ***p<0.001. (C) CAB staining of the SMGs from P28 and P56 male WT and *Insig1/2* cKO mice. Scale bars; 25 μm in top and bottom panels, and 100 μm in middle panels. (D) Gross picture of the testes from P56 WT control and *Insig1/2* cKO mice. (E) The percentage of testis weight per body weight at P56. WT: blue bar, cKO: red bar. n=6 per group. (F) Quantitative RT-PCR analyses for the indicated genes in the SMGs of P56 male WT control (blue bars) and *Insig1/2* cKO (red bars) mice. n=6 per group. ***p<0.001. (G) Immunohistochemical analysis for NGF expression (green) in the SMGs of P56 male WT control and *Insig1/2* cKO mice. Nuclei were stained with DAPI (blue). Scale bars; 50 μm. (H) Immunohistochemical analysis for EGF expression (green) in the SMGs of P56 male WT control and *Insig1/2* cKO mice. Nuclei were stained with DAPI (blue). Scale bars; 50 μm.
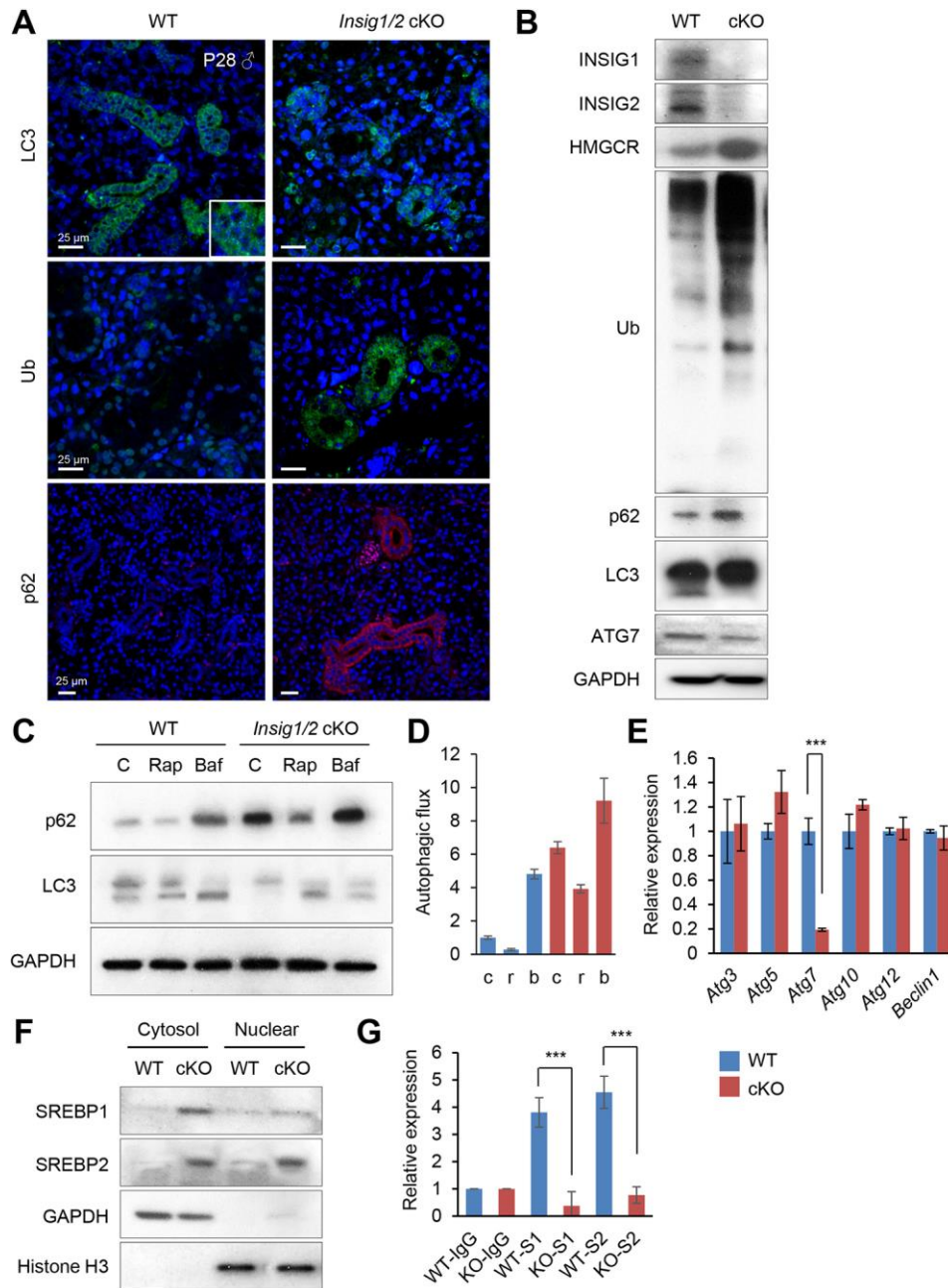
Fig. 2. Impaired autophagy during development of the submandibular glands in *Insig1/2* cKO mice.

(A) Immunohistochemical analysis of LC3 (green), ubiquitin (Ub, green), and p62 (red) in the SMGs of P28 male wild-type (WT) and *Insig1/2* cKO mice. Nuclei were stained with DAPI (blue). Scale bars, 25 μm. (B) Immunoblotting for the indicated molecules in the SMGs of P28 male WT and *Insig1/2* cKO mice. (C) Immunoblotting for the indicated molecules, after treatment with vehicle control (C), 100 nM rapamycin (Rap), and 200 nM bafilomycin (Baf) for 24 hours, in SMG explants from WT and *Insig1/2* cKO mice. (D) Autophagic flux was measured through quantification of three independent blots for p62 after treatment with control vehicle (c), rapamycin (r), and bafilomycin (b) in WT (blue bars) and *Insig1/2* cKO (red bars) mice. (E) Quantitative RT-PCR analyses for genes related to the autophagic machinery in the submandibular glands of P56 WT control (blue bars) and *Insig1/2* cKO (red bars) mice. n=6 per group. *** $p<0.001$. (F) Cell fractionation and subsequent immunoblotting for the indicated molecules in the SMGs of P28 male WT and *Insig1/2* cKO mice. (G) ChIP assays of IgG control and SREBP1 (S1) or SREBP2 (S2) for a SREBP-binding site in the *Atg7* promoter region in wild-type (WT; blue bars) control and *Insig1/2* conditional knockout (KO; red bars) SMGs. n=6 per group. *** $p<0.001$.
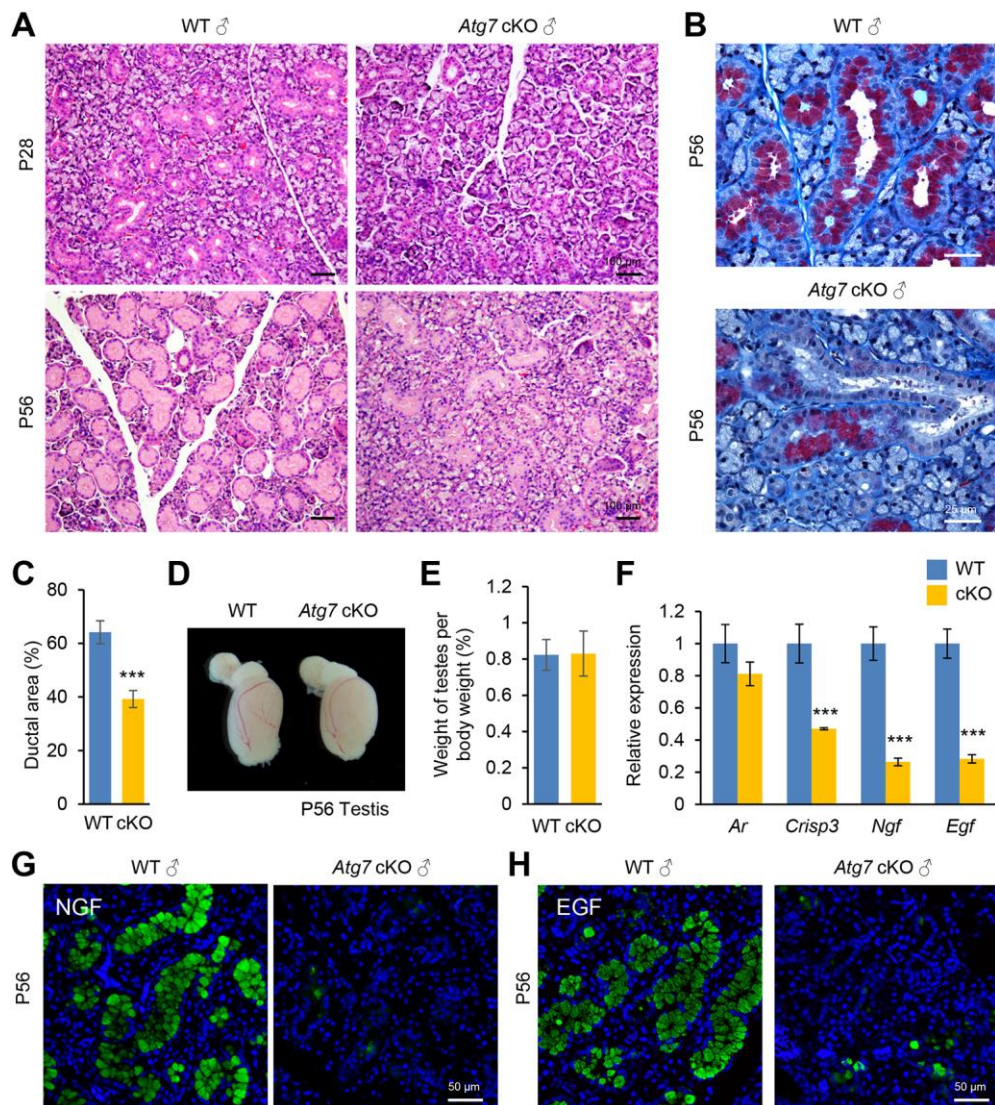
Fig. 3. Phenotypic analyses of salivary glands of *Atg7^{F/F};K14-Cre* cKO male mice.

(A) H&E staining of the SMGs from P28 and P56 male wild-type (WT) control and *Atg7* cKO

mice. Scale bars; 100 μm. (B) CAB staining of the SMGs from P56 male WT and *Atg7* cKO mice.

Scale bars; 25 μm. (C) Quantification of ductal area per total gland area in the SMGs of P56 male

WT (blue bar) and *Atg7* cKO (yellow bar) mice. n=6 per group. ***p<0.001. (D and E) Gross

picture (D) of the testes and percentage of testis weight per body weight (E, n=6 per group) for

P56 WT control (blue bar) and *Atg7* cKO (yellow bar) mice. (F) Quantitative RT-PCR analyses

for the indicated genes in the SMGs of P56 male WT control (blue bars) and *Atg7* cKO (yellow

bars) mice. n=6 per group. ***p<0.001. (G) Immunohistochemical analysis for NGF expression

(green) in the SMGs of P56 male WT control and *Atg7* cKO mice. Nuclei were stained with DAPI

(blue). Scale bars; 50 μm. (H) Immunohistochemical analysis for EGF expression (green) in the

SMGs of P56 male WT control and *Atg7* cKO mice. Nuclei were stained with DAPI (blue). Scale
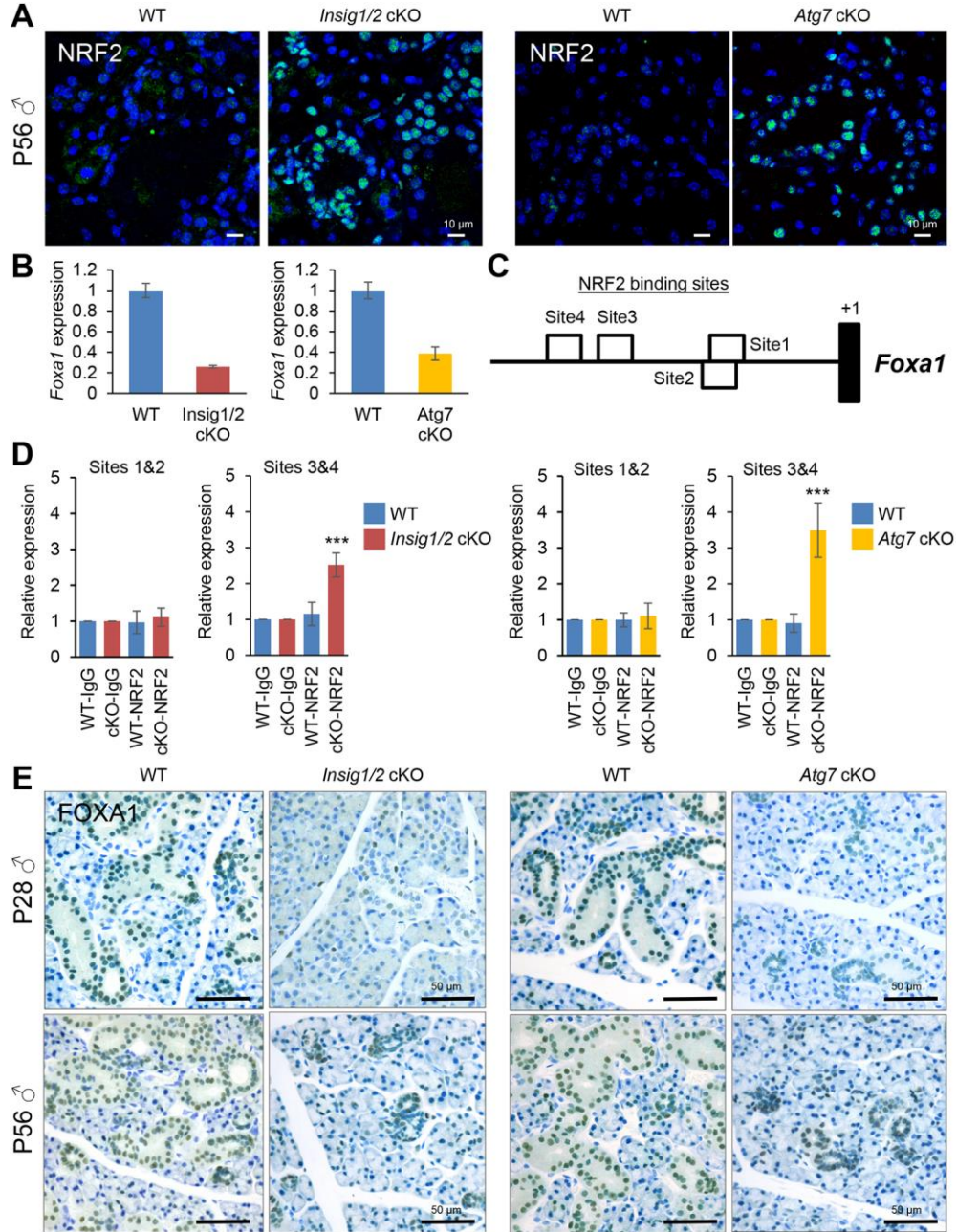
bars; 50 μm.

Fig. 4. Compromised *Foxa1* expression during GCT maturation in *Insig1/2* cKO and *Atg7* cKO mice.

(A) NRF2 expression in wild-type (WT), *Insig1/2* cKO (left), and *Atg7* cKO (right) GCTs of male mice at P56. Nuclei were stained with DAPI (blue). Scale bars; 10 μm. (B) Quantitative RT-PCR analyses of *Foxa1* expression in the SMGs of male WT (blue bars), *Insig1/2* cKO (red bar), and *Atg7* cKO (green bar) mice at P28 and P56. n=6 per group. ***$p<0.001$. (C) Schematic drawing of the *Foxa1* promoter. (D) ChIP assays for NRF2 binding to the NRF2-binding sites in the *Foxa1* promotor region, using SMG tissues from P56 male WT control (blue bars), *Insig1/2* cKO (red bars), and *Atg7* cKO (green bars) mice. n=6 per group. ***$p<0.001$. (E) Immunohistochemical analysis for FOXA1 (brown) in the SMGs of male WT, *Insig1/2* cKO, and *Atg7* cKO mice at P28 and P56. Nuclei were stained with 0.04% methylene blue. Scale bars; 50 μm.
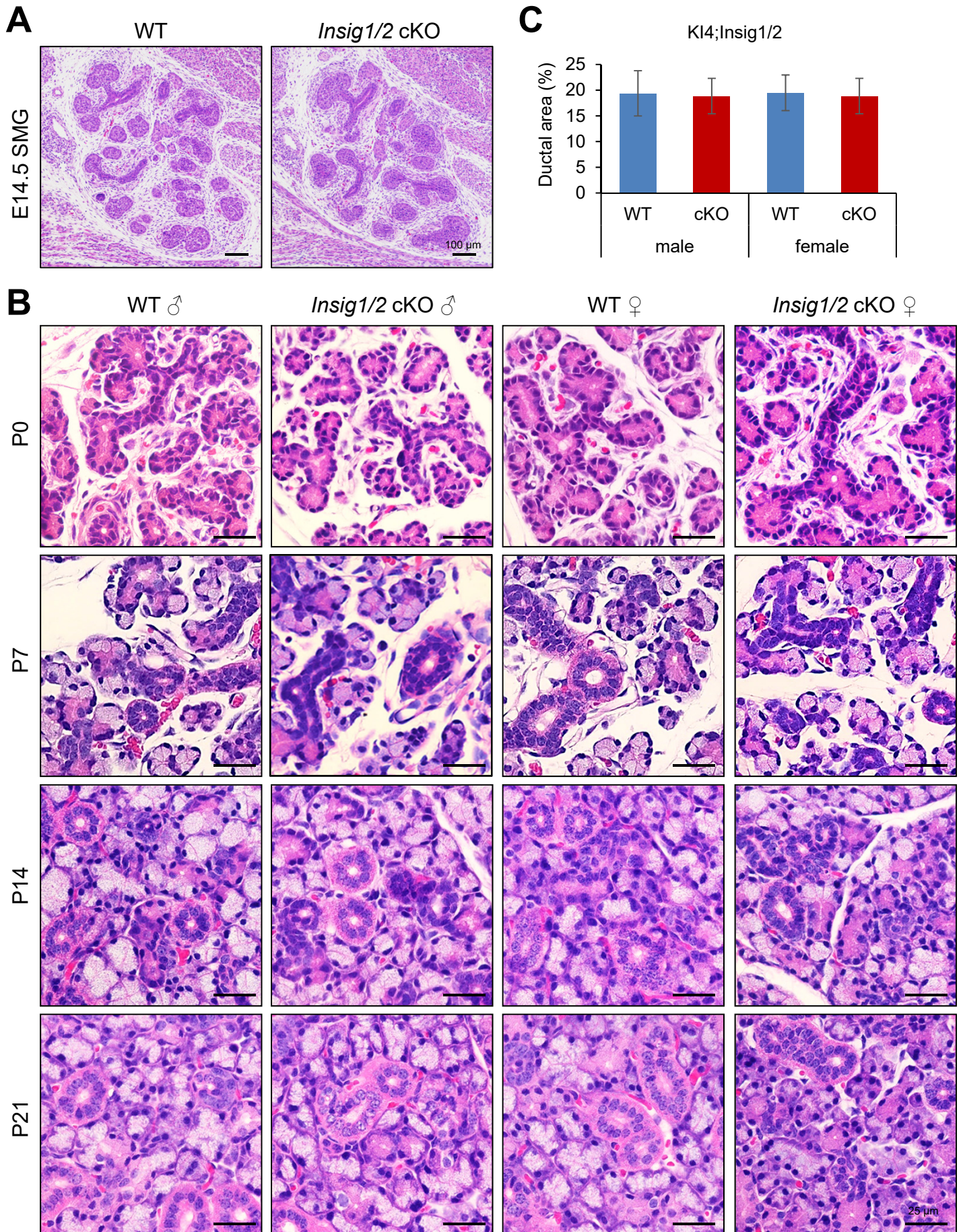
A

WT | *Insig1/2* cKO

E14.5 SMG

100 µm

C

KI4;Insig1/2

Ductal area (%)

WT | cKO | WT | cKO
male | | female |

B

WT ♂ | *Insig1/2* cKO ♂ | WT ♀ | *Insig1/2* cKO ♀

P0

P7

P14

P21

25 µm

Fig. S1. No developmental defects in *Insig1/2* cKO SMG before P21.

(A) H&E staining images of E14.5 SMGs from wild-type (WT) control and *Insig1/2* cKO embryos. Scale bars, 100 μm. (B) H&E staining images of SMGs from male and female WT control and *Insig1/2* cKO mice right after birth (P0), and at P7, 14, and 21 days. Scale bars, 25 μm. (C) Quantification of ductal area per total gland area in P21 SMGs of male and female WT (blue bars) and *Insig1/2* cKO (red bars) mice. n=10 images (x40) per group.
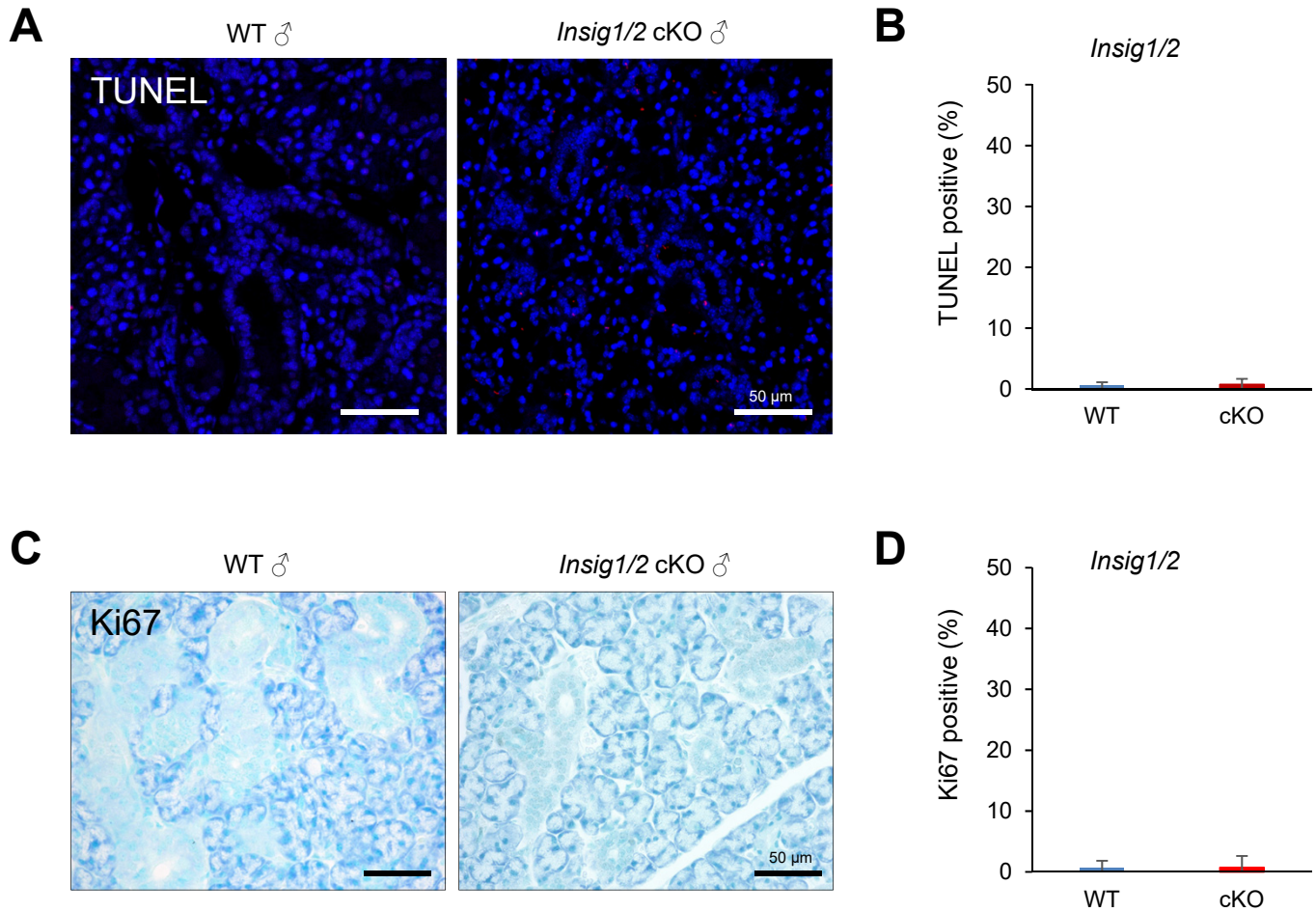
Fig. S2. No alternation in cell death and proliferation in *Insig1/2* cKO SMG.

(A) TUNEL staining in the SMGs of male WT and *Insig1/2* cKO mice at 8 weeks of age. Scale

bars, 50 μm. (B) Quantification of TUNEL-positive (red) cells in (A). n=10 images (x40) per group.

(C) Immunostaining for Ki67 in the SMGs of male WT and *Insig1/2* cKO mice at 8 weeks of age.

Scale bars, 50 μm. (D) Quantification of Ki67-positive cells in (C). n=10 images (x40) per group.

Fig. S3. Increased cholesterol synthesis causes GCT maturation defects.

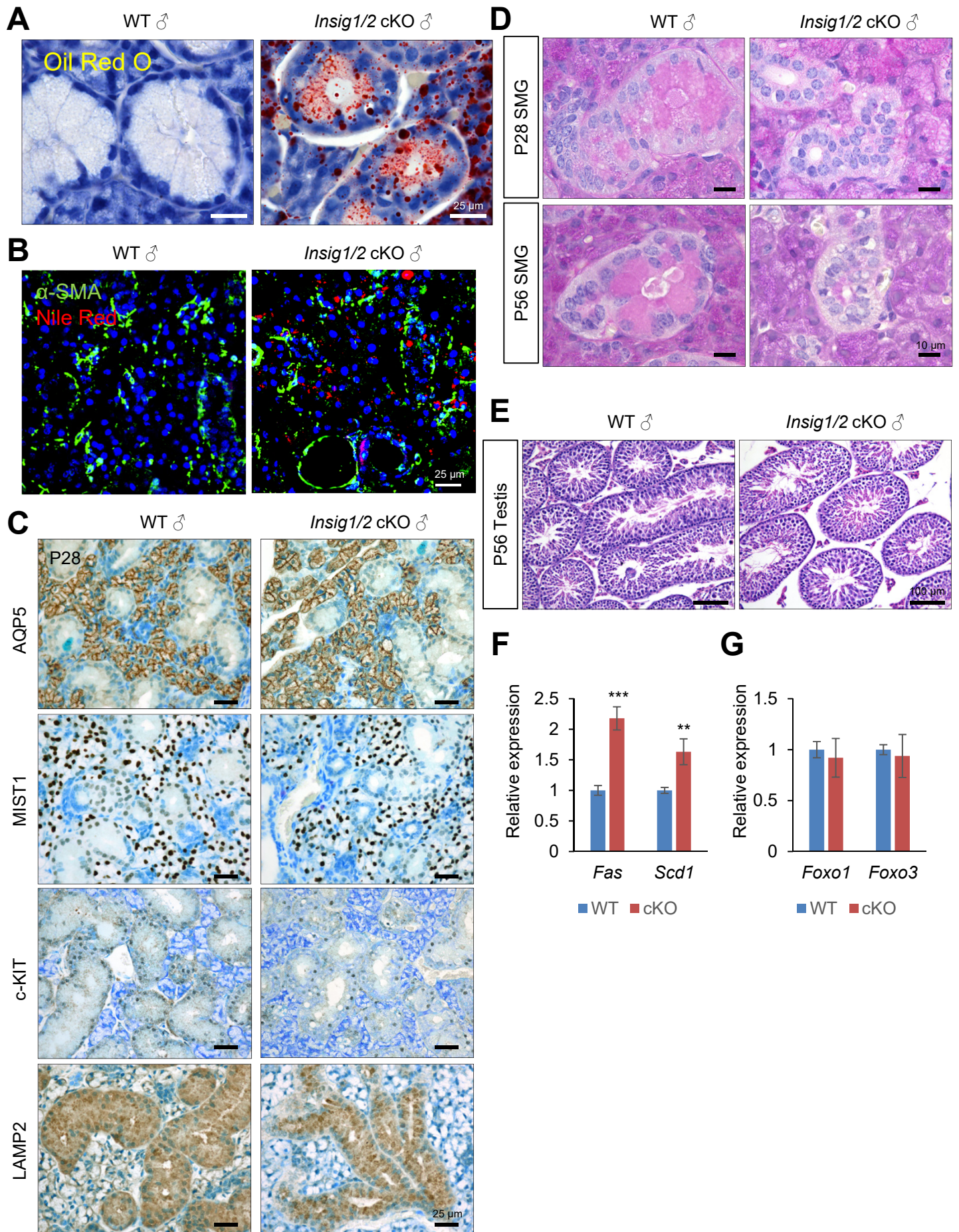(A) Oil Red O staining in the SMGs of male WT and *Insig1/2* cKO mice at 8 weeks of age. 0.04% methylene blue was used for counterstaining. Scale bars, 25 μm. (B) Immunohistochemical staining for α-SMA (green) and Nile Red (red) in the SMGs of male WT and *Insig1/2* cKO mice at 8 weeks of age. DAPI (blue) was used for nuclear staining. Scale bars, 25 μm. (C) Immunohistochemical staining for the indicated molecules (brown) in the SMGs of male WT and *Insig1/2* cKO mice at 8 weeks of age. 0.04% methylene blue was used for counterstaining. Scale bars, 25 μm. (D) PAS staining in the SMGs of male WT and *Insig1/2* cKO mice at P28 and P56. 0.04% methylene blue was used for counterstaining. Scale bars, 10 μm. (E) Hematoxylin and Eosin staining of the testes of P56 male WT and *Insig1/2* cKO mice. Scale bars, 100 μm. (F, G) Quantitative RT-PCR for the indicated genes in the SMGs of male WT (blue bars) and *Insig1/2* cKO (red bars) mice at 8 weeks of age. **$p<0.01$. ***$p<0.001$.
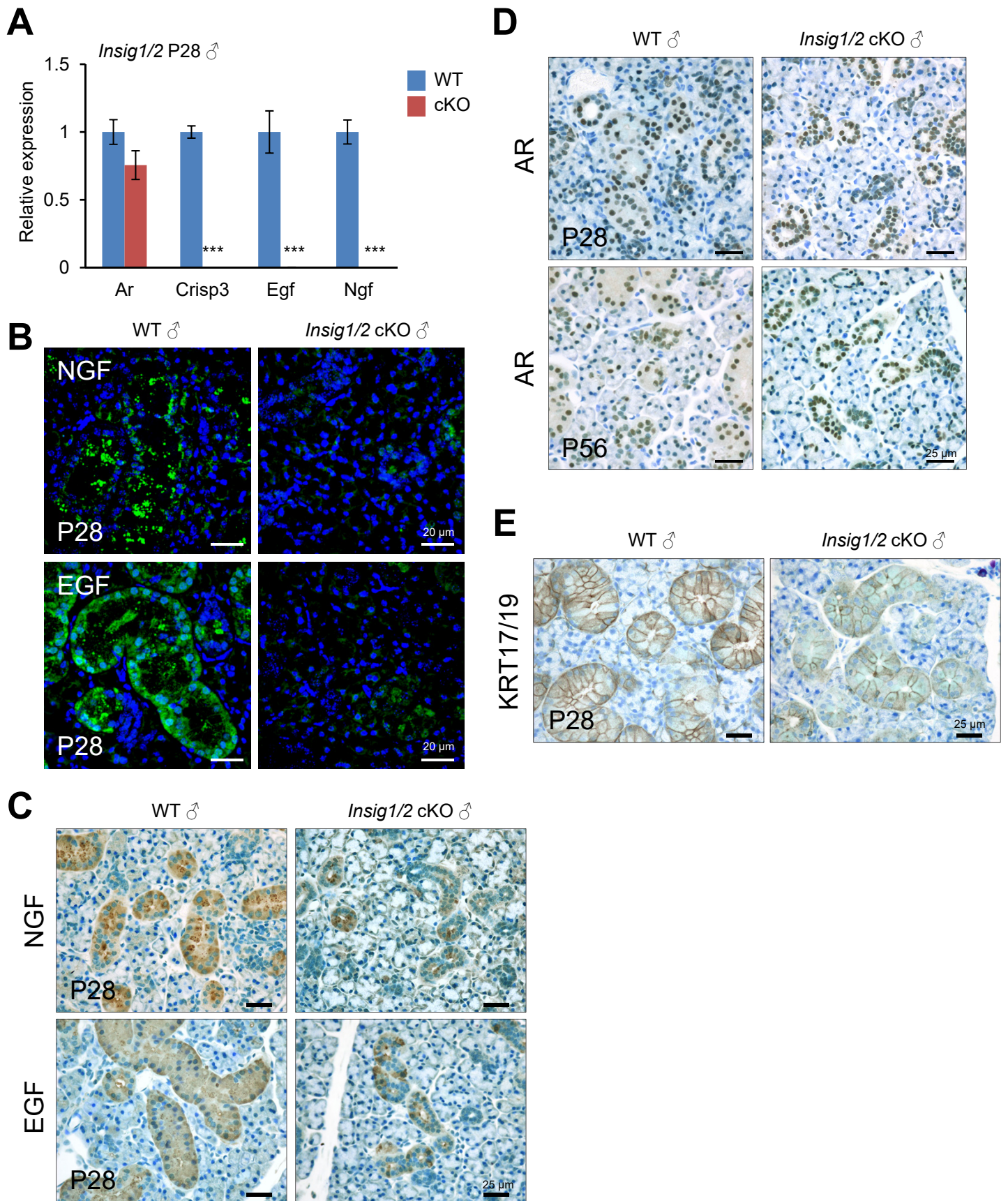
Fig. S4. Compromised AR signaling in the SMGs of *Insig1/2* cKO mice.

(A) Quantitative RT-PCR analyses for the indicated genes in the SMGs of P28 male wild-type (WT) control (blue bars) and *Insig1/2* cKO (red bars) mice. n=6 per group. ***p<0.001. (B) Immunohistochemical staining (green) for NGF and EGF in the SMGs of P28 male WT control and *Insig1/2* cKO mice. DAPI (blue) was used for nuclear staining. Scale bars; 20 μm. (C-E) Immunohistochemical staining of the indicated molecules (brown) in the SMGs of male wild-type (WT) and *Insig1/2* cKO mice at P28 and P56. Nuclei were counterstained with 0.04% methylene blue. Scale bars, 25 μm.
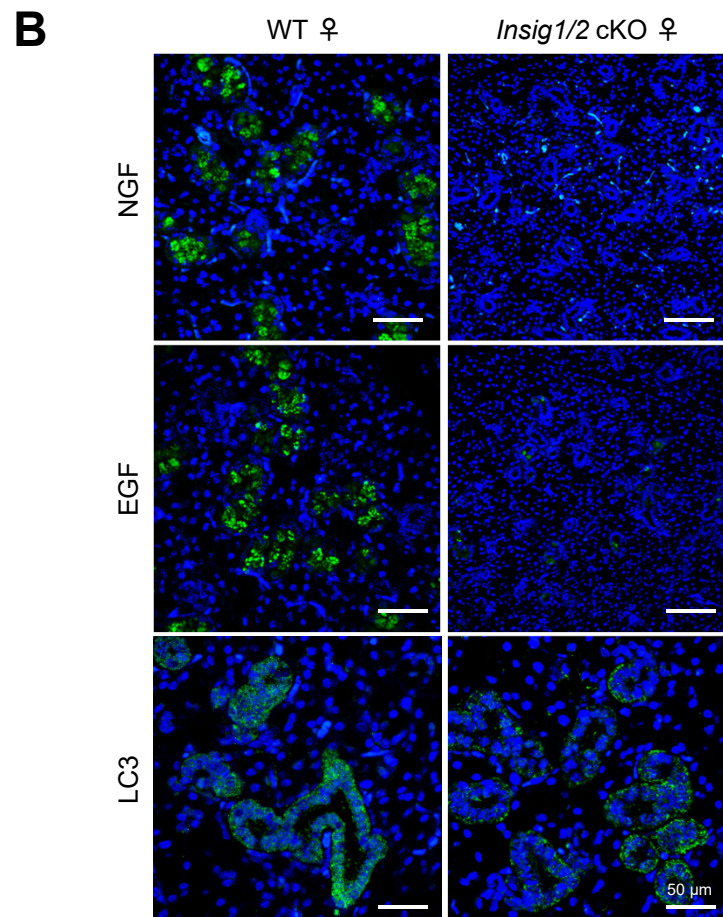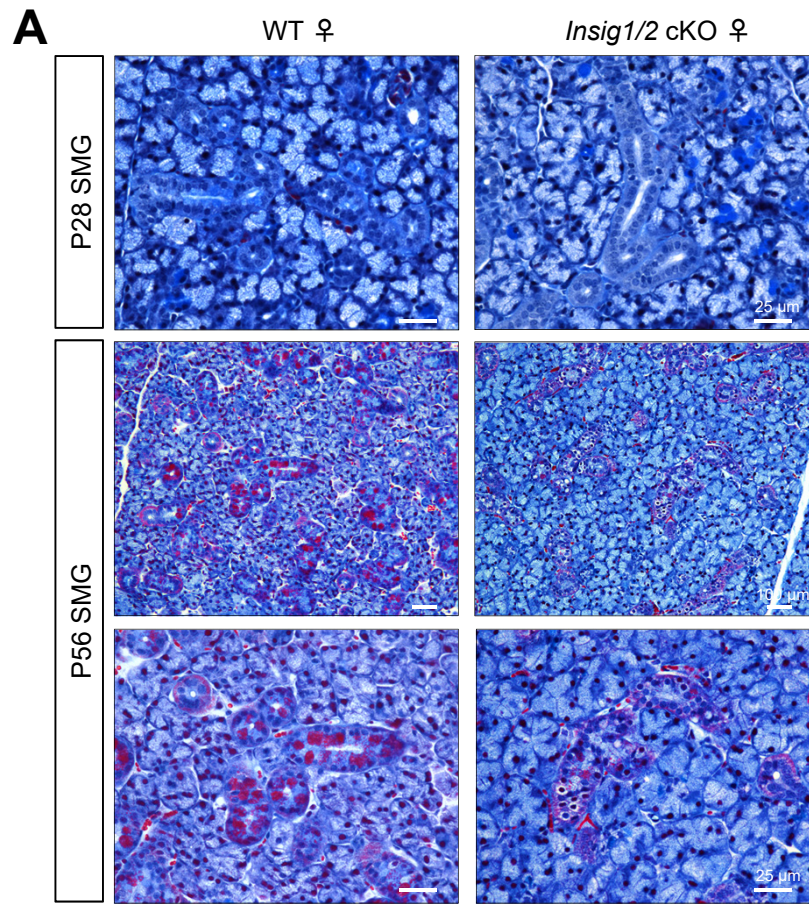
Fig. S5. GCT maturation defects in the SMGs of female *Insig1/2* cKO mice.

(A) CAB staining in the SMGs of female wild-type (WT) and *Insig1/2* cKO mice at P28 and P56.

Scale bars; 25 μm in top and bottom panels, and 100 μm in middle panels. (B)

Immunohistochemical staining for NGF, EGF, and LC3 (green) in the SMGs of female WT and

Insig1/2 cKO mice at P56. DAPI (blue) was used for nuclear staining. Scale bars, 50 μm.

A

E14.5 SMG

WT   *Atg7* cKO

100 µm

C

KI4;Atg7

Ductal area (%)

WT   cKO   WT   cKO
male   female

B

WT ♂   *Atg7* cKO ♂   WT ♀   *Atg7* cKO ♀

P0

P7

P14

P21

25 µm
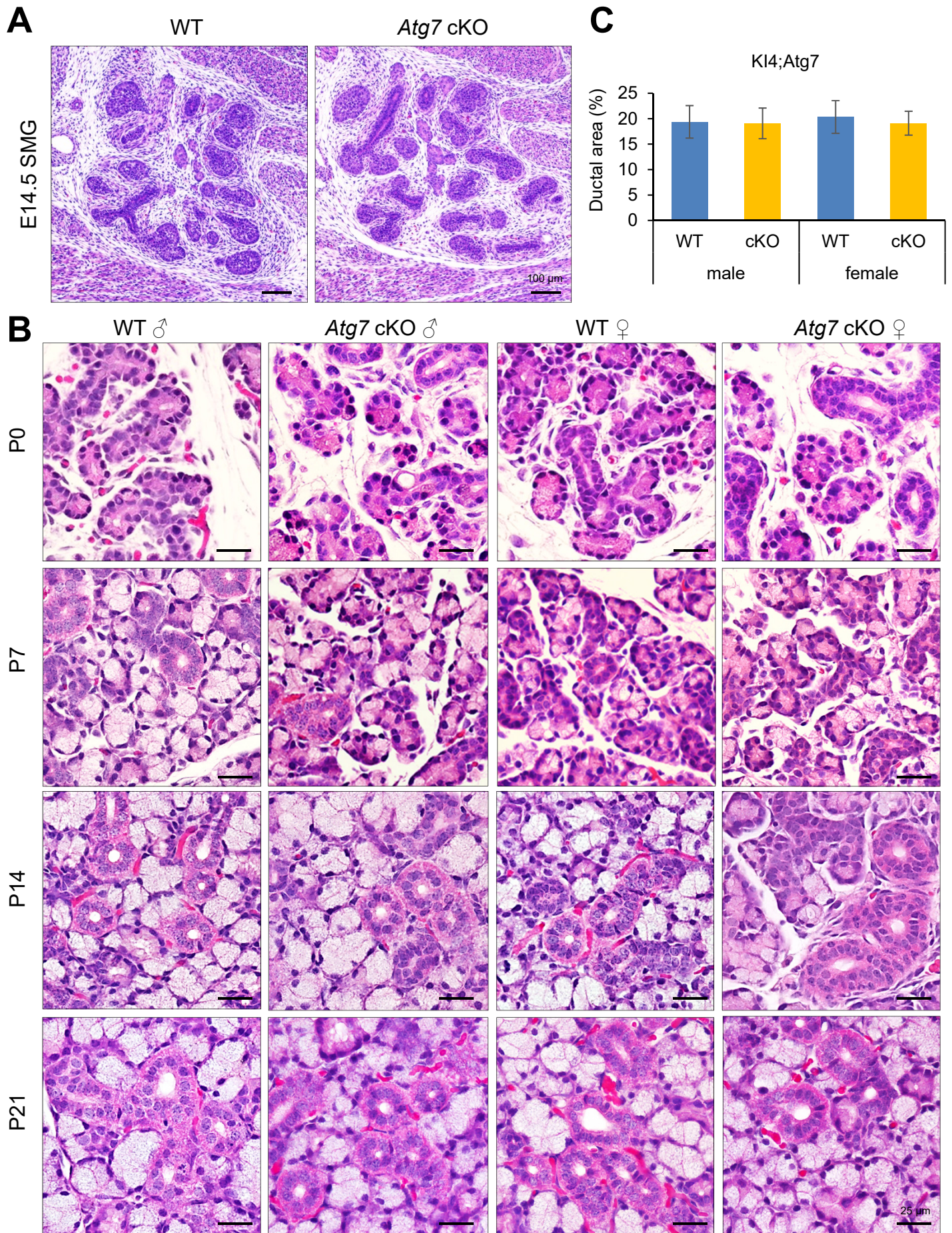
Fig. S6. Normal early-stage SMG development in *Atg7* cKO mice.

(A) H&E staining images of E14.5 SMGs of wild-type (WT) control and *Atg7* cKO embryos. Scale bars, 100 μm. (B) H&E staining of the SMGs of male and female WT control and *Insig1/2* cKO mice at postnatal day (P) day 0 (P0), P7, P14, and P21. Scale bars, 25 μm. (C) Quantification of ductal area per total gland area in the SMGs of P21 male and female WT (blue bars) and *Atg7* cKO (yellow bars) mice. n=10 images per group.
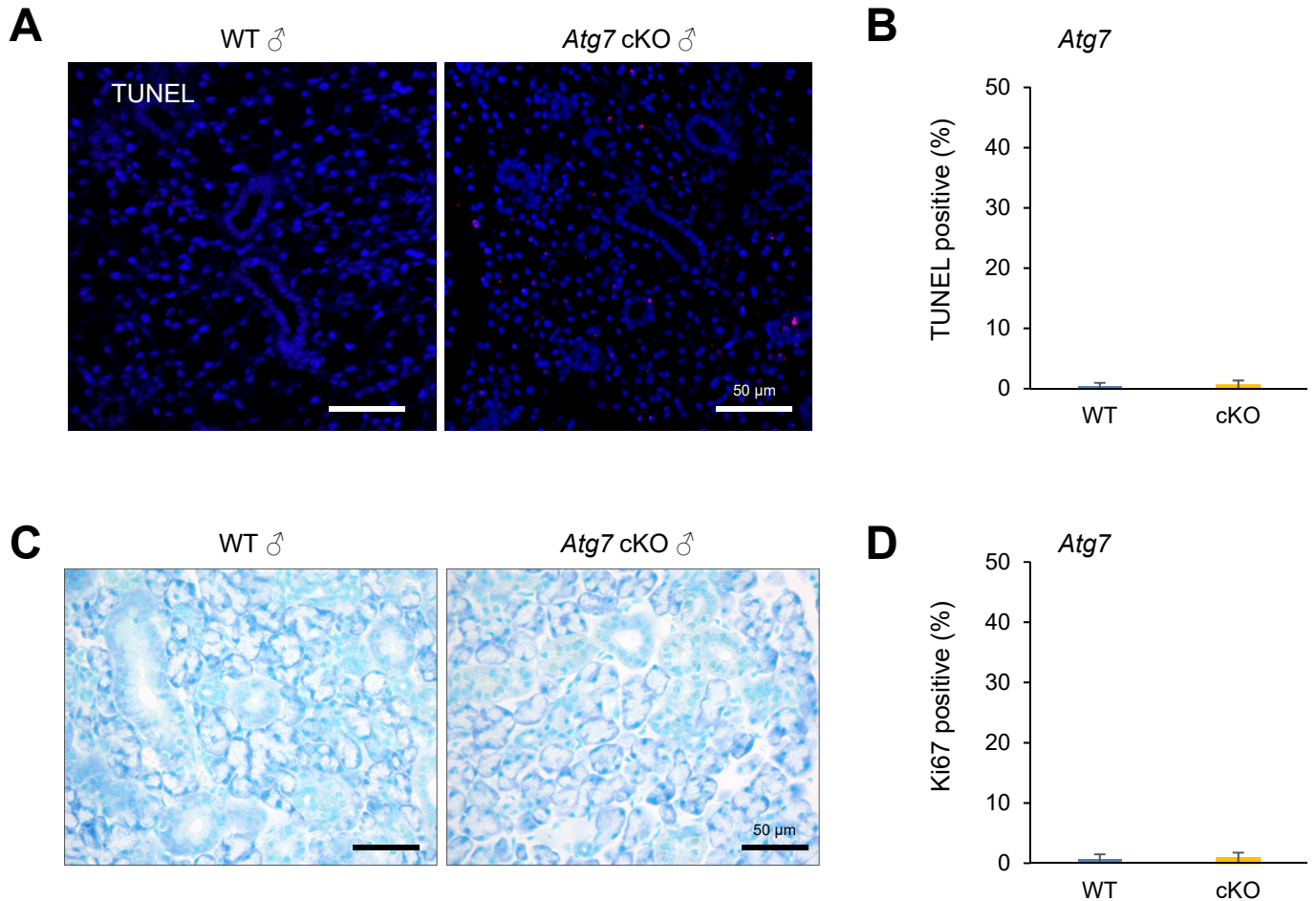
Fig. S7. No alternation in cell death and proliferation in *Atg7* cKO SMG.

(A) TUNEL staining (red) in the SMGs of male WT and *Atg7* cKO mice at 8 weeks of age. Scale bars, 50 μm. (B) Quantification of TUNEL-positive cells in (A). n=10 images (x40) per group. (C) Immunostaining for Ki67 (brown) in the SMGs of male WT and *Atg7* cKO mice at 8weeks of age. 0.04% methylene blue was used for counterstaining. Scale bars, 50 μm. (D) Quantification of Ki67-positive cells in (C). n=10 images (x40) per group.

Fig. S8. Maturation defect in the GCTs of *Atg7* cKO male mice.

(A) CAB staining in the SMGs of male wild-type (WT) and *Atg7* cKO mice at P28 and P56. Scale

bars, 25 μm. (B) PAS staining in the SMGs of male WT and *Atg7* cKO mice at P28 and P56.

Hematoxylin was used for counterstaining. Scale bars, 10 μm. (C) Immunohistochemical staining

for the indicated molecules in the SMGs of male WT and *Atg7* cKO mice at P56. 0.04% methylene

blue was used for counterstaining. Scale bars, 25 μm. (D) Immunohistochemical staining for α-

SMA (green) and Nile Red (red) in the SMGs of male WT and *Atg7* cKO mice at 8 weeks of age.

DAPI (blue) was used for nuclear staining. Scale bars, 25 μm. (E) Oil Red O staining in the SMGs

of male WT and *Atg7* cKO mice at 8 weeks of age. 0.04% methylene blue was used for

counterstaining. Scale bars, 25 μm. (F) Hematoxylin and Eosin staining of the testis of P56 male

WT and *Atg7* cKO mice. Scale bars, 100 μm. (G) Quantitative RT-PCR for the indicated genes in

the SMGs of male WT (blue bars) and *Atg7* cKO (yellow bars) mice at 8 weeks of age.
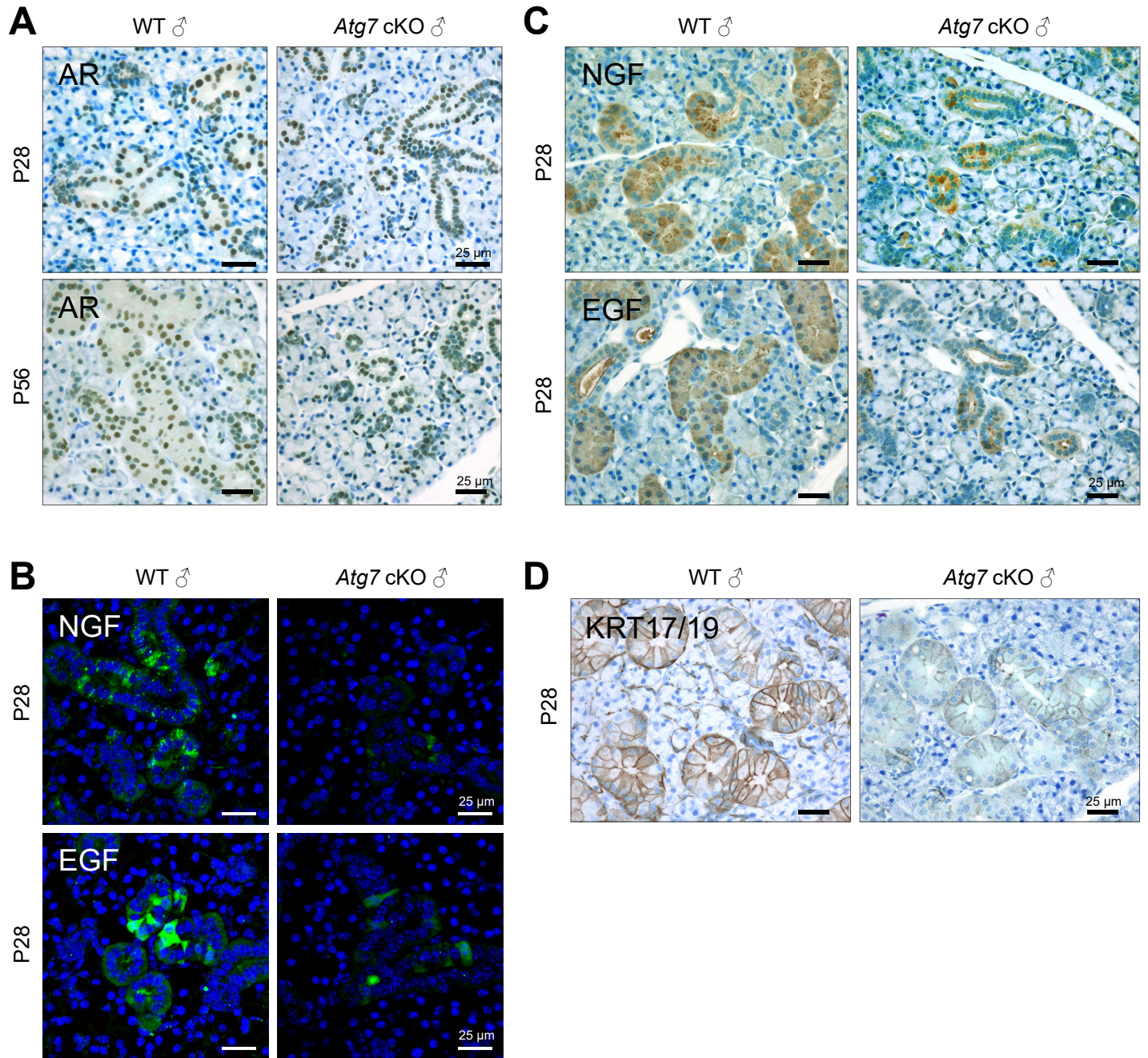
Fig. S9. Suppressed AR signaling in the GCTs of *Atg7* cKO mice.

(A) Immunohistochemical staining for AR (brown) in the SMGs of male wild-type (WT) control and *Atg7* cKO mice. Nuclei were stained with 0.04% methylene blue. Scale bars, 25 μm. (B) Immunohistochemical staining for NGF and EGF in the SMGs of P28 WT control and *Atg7* cKO mice. Nuclei were stained with DAPI (blue). Scale bars, 25 μm. (C, D) Immunohistochemical staining for the indicated molecules in the SMGs of P28 WT control and *Atg7* cKO mice. Nuclei were stained with 0.04% methylene blue. Scale bars, 25 μm.
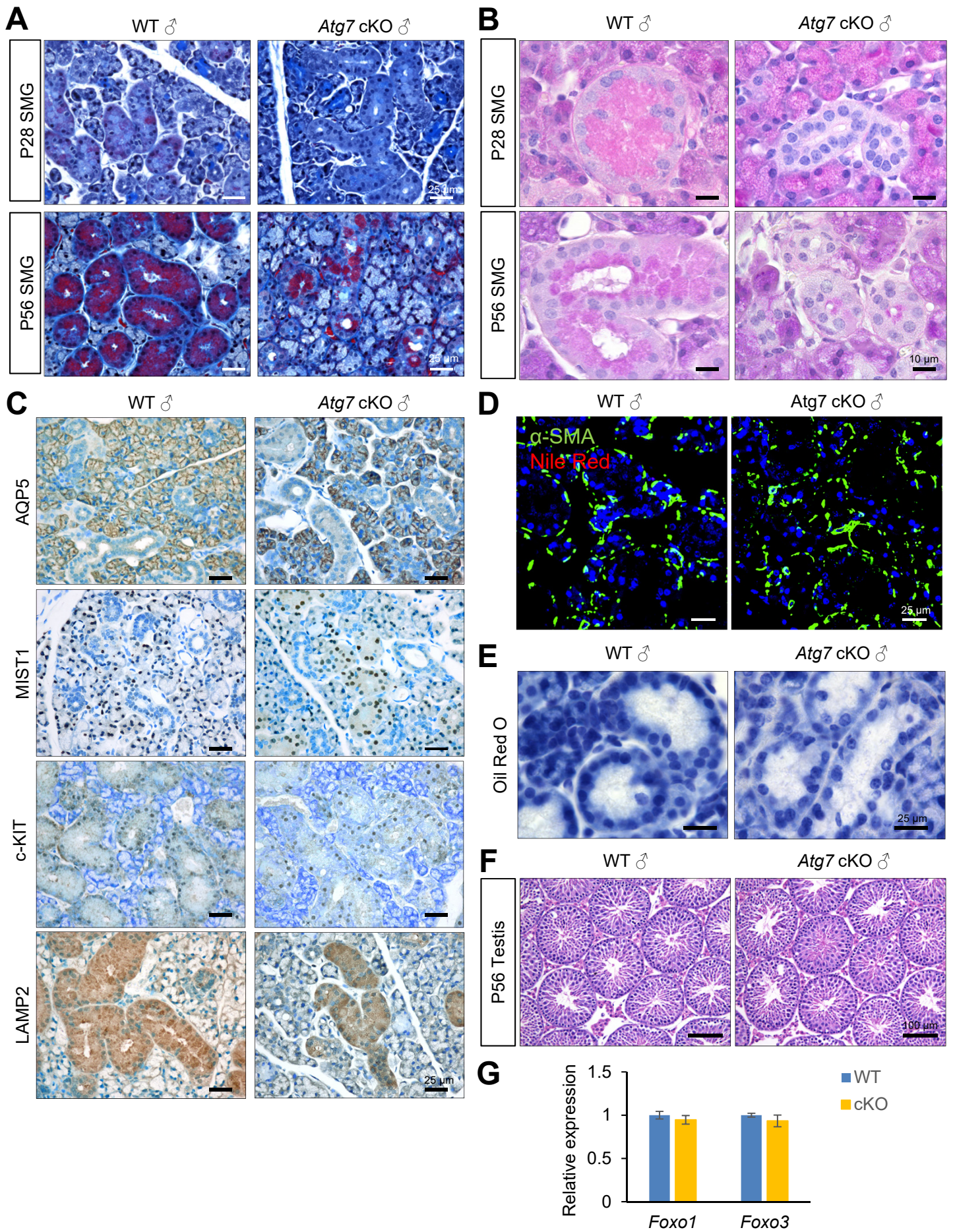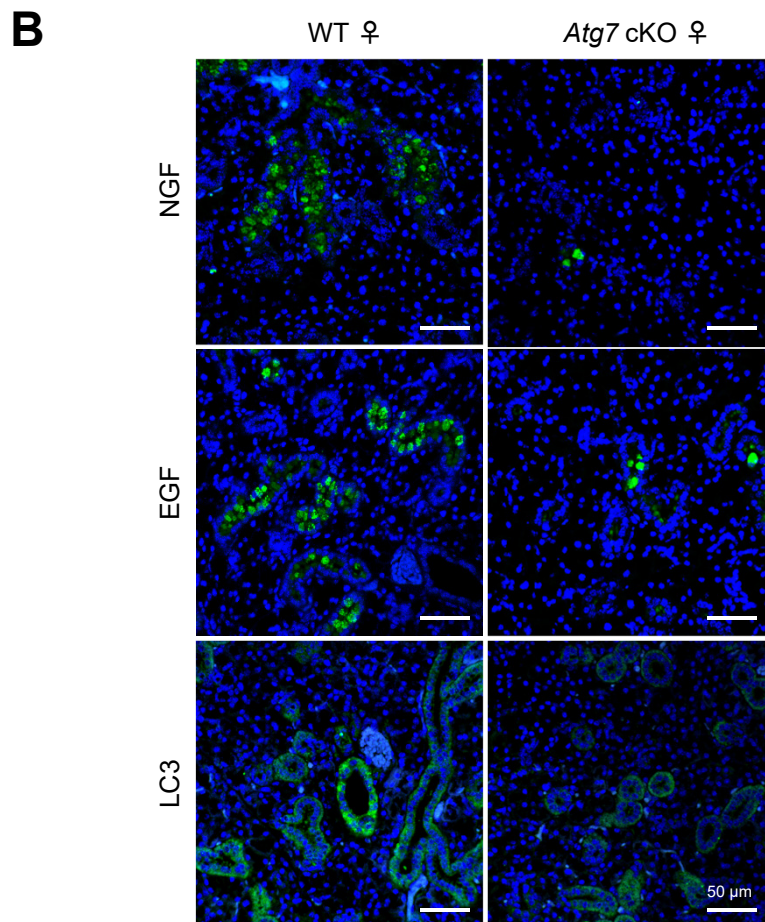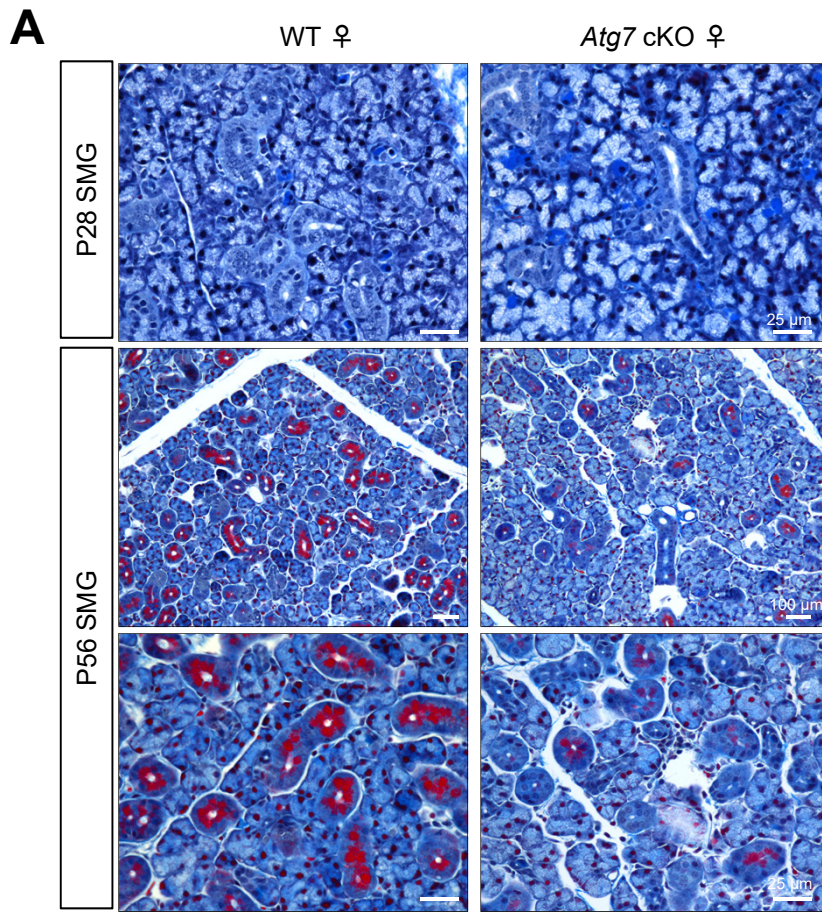
Fig. S10. GCT maturation defects in the SMGs of female *Atg7* cKO mice.

(A) CAB staining in the SMGs of female wild-type (WT) and *Atg7* cKO mice at P28 and P56.

Scale bars; 25 μm in top and bottom panels, and 100 μm in middle panels. (B)

Immunohistochemical staining for NGF, EGF, and LC3 (green) in the SMGs of female WT and

Atg7 cKO mice at P56. DAPI (blue) was used for nuclear staining. Scale bars, 50 μm.
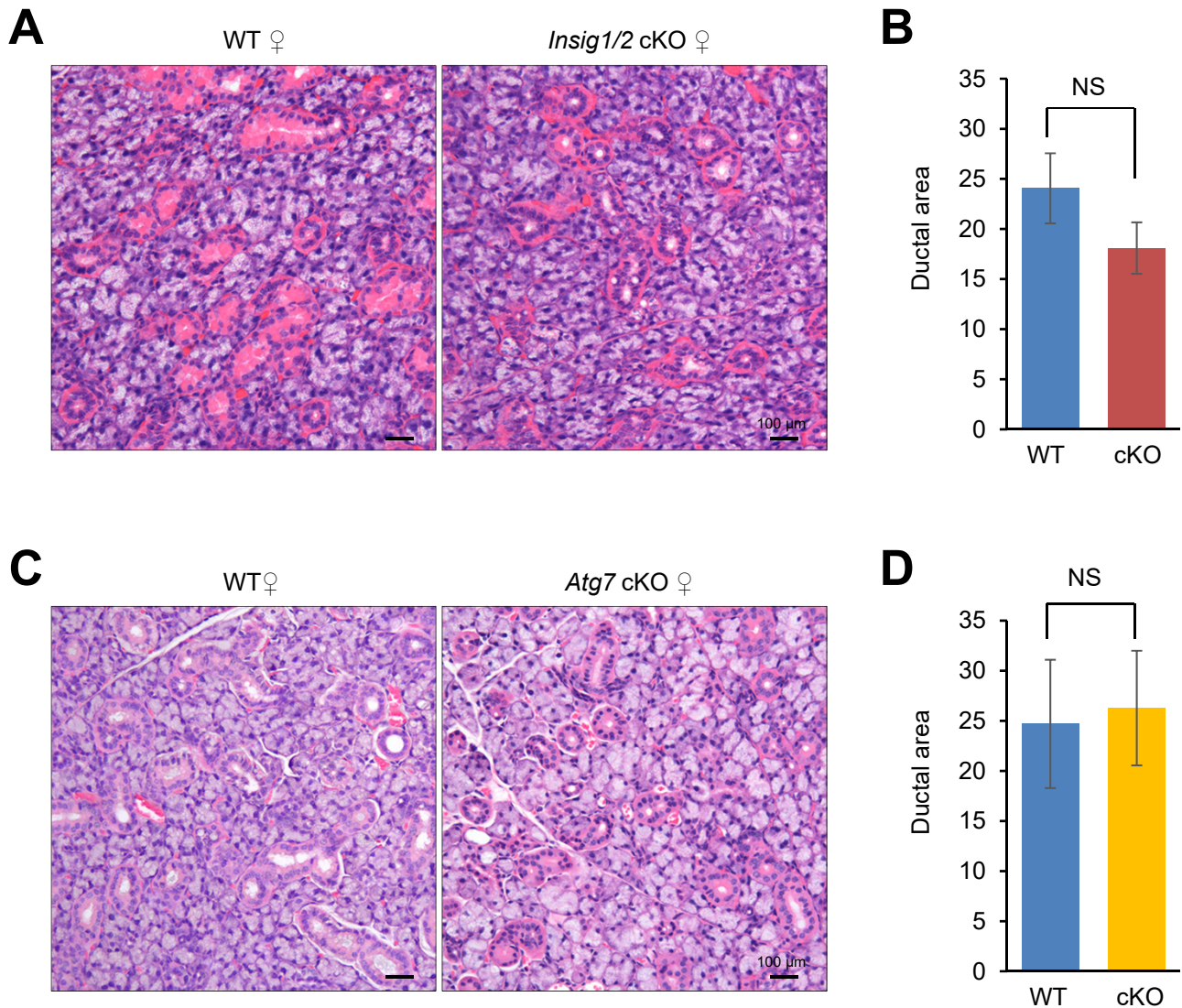
Fig. S11. No developmental defects in the SMGs of female *Insig1/2* cKO and *Atg7* cKO mice.

(A) H&E staining of the SMGs from P56 wild-type (WT) female control and *Insig1/2* cKO mice. Scale bars, 100 μm. (B) Quantification of ductal area per total gland area in the SMGs of P56 female WT (blue bar) and *Insig1/2* cKO (red bar) mice. n=10 images (x40) per group. NS: not significant. (C) H&E staining of the SMGs from P56 female WT control and *Atg7* cKO mice. Scale bars, 100 μm. (D) Quantification of ductal area per total gland area in the SMGs of P56 female WT (blue bar) and *Atg7* cKO (yellow bar) mice. n=10 images (x40) per group. NS: not significant.
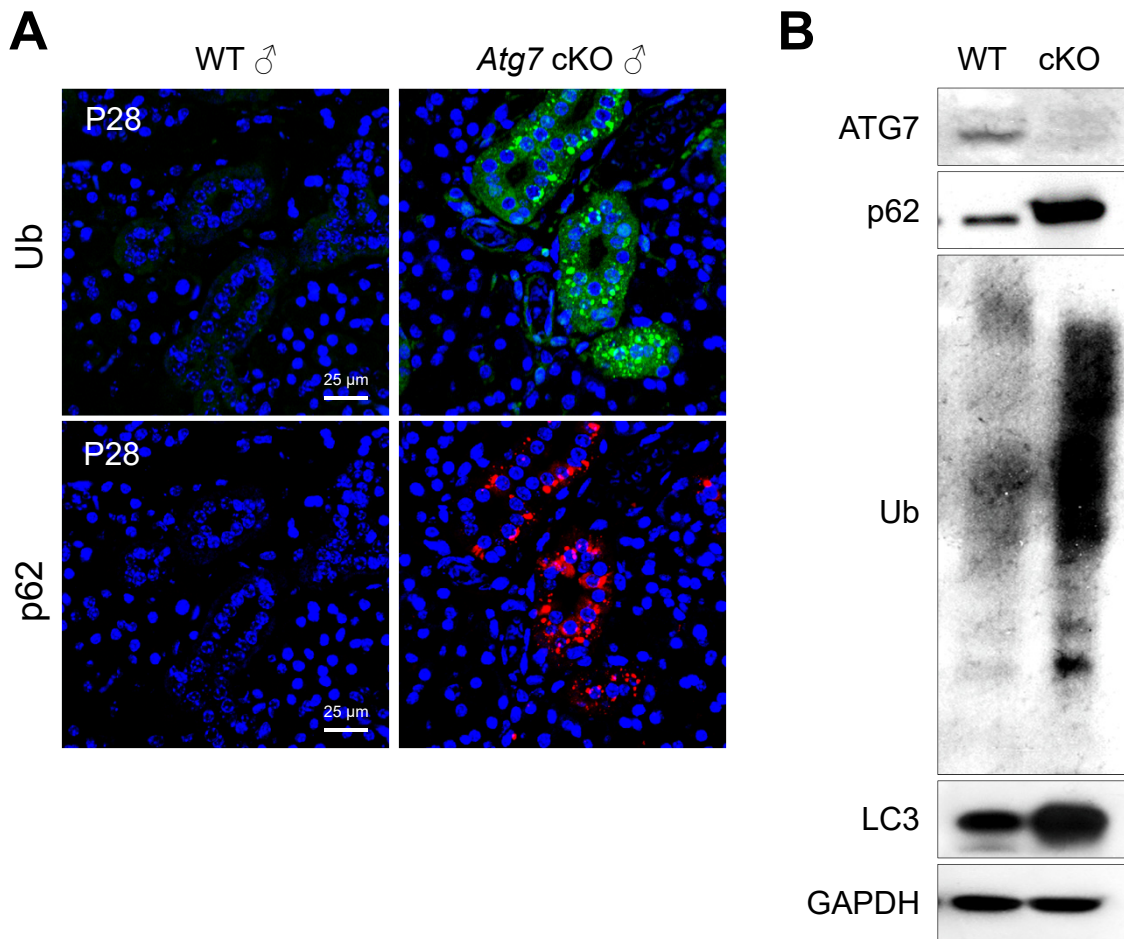
Fig. S12. Impaired autophagic machinery during GCT maturation in *Atg7* cKO mice.

(A) Immunohistochemical staining for ubiquitin (Ub: green) and p62 (red) in the SMGs of P28 male wild-type (WT) and *Atg7* cKO mice. Nuclei were stained with DAPI (blue). Scale bars, 25 μm. (B) Immunoblotting for the indicated molecules in the SMGs of P28 male WT and *Atg7* cKO mice.

A

GAPDH normalization

β-actin normalization

Insig1/2 4w SMG

B

GAPDH normalization

β-actin normalization

Atg7 4w SMG

Fig. S13. No difference in the ER stress markers.

(A) Quantitative RT-PCR for the indicated molecules in the SMGs of P28 male WT (blue bars) and *Insig1/2* cKO (red bars) mice. (B) Quantitative RT-PCR for the indicated molecules in the SMGs of P28 male WT (blue bars) and *Atg7* cKO (yellow bars) mice.

ARE sites 1 and 2

```
Dog          gtctccactctgctagccaggagcccagataggcctaacgtcactcggctaggttgactcaga
Horse        gtctccactctgctagccaggagcccggatcggcctaacgtcactcggctcggctgactcaga
Macaque      gcctccgctctgctagccgggagcccgggtcggcctaacgtcacttggctcggctgactcaga
Orangutan    gcctccgctctgctagcccggggcccgggtcggcctaacgtcacttggctcggctgactcaga
Human        gcctccgctctgctagcccggggcccgggtcggcctaacgtcacttggctcggctgactcaga
Chimpanzee   gcctccgctctgctagcccggggcccgggtcggcctaacgtcacttggctcggctgactcaga
Mouse        gcctccgttctgctcgccaggagcccaggtcggcctaacgtcactttgctcggctgactcaga
Rat          gcctccgttctgctagccaggagcccaggtcggcctaacgtcactctgcttggctgactcaga
             * ****  ****** *** ** **** * * *************  *** ** *********
                                                                    Site1
                                                                    Site2
```

ARE site 3

```
Dog          gatataaaacggtgctgtgactcacctgctcttagccgcaggtacgggtttcgtggcagc
Horse        gatataaaacggtgccgtgactcacctgctcttagccgcaggtatgggtttcgtggcagc
Macaque      gatataaaccggtgctgtgactcacctgctcttagccgcaggtacgagtttcgtggcagc
Orangutan    gatataaaccggtgctgtgactcacctgctcttagccgcaggtacgagtttcgtggcagc
Human        gatataaaccggtgctgtgactcacctgctcttagccgcaggtacgagtttcgtggcagc
Chimpanzee   gatataaaccggtgctgtgactcacctgctcttagccgcaggtacgagtttcgtggcagc
Mouse        aatataaaacggtgctgtgactcacctgctcttagccgcaggtacgagtttcgtggcagc
Rat          aatataaaacggtgctgtgactcacctgctcttagccgcaggtacgagtttcgtggcagc
             ******* ****** **************************** * ************
                              Site3
```
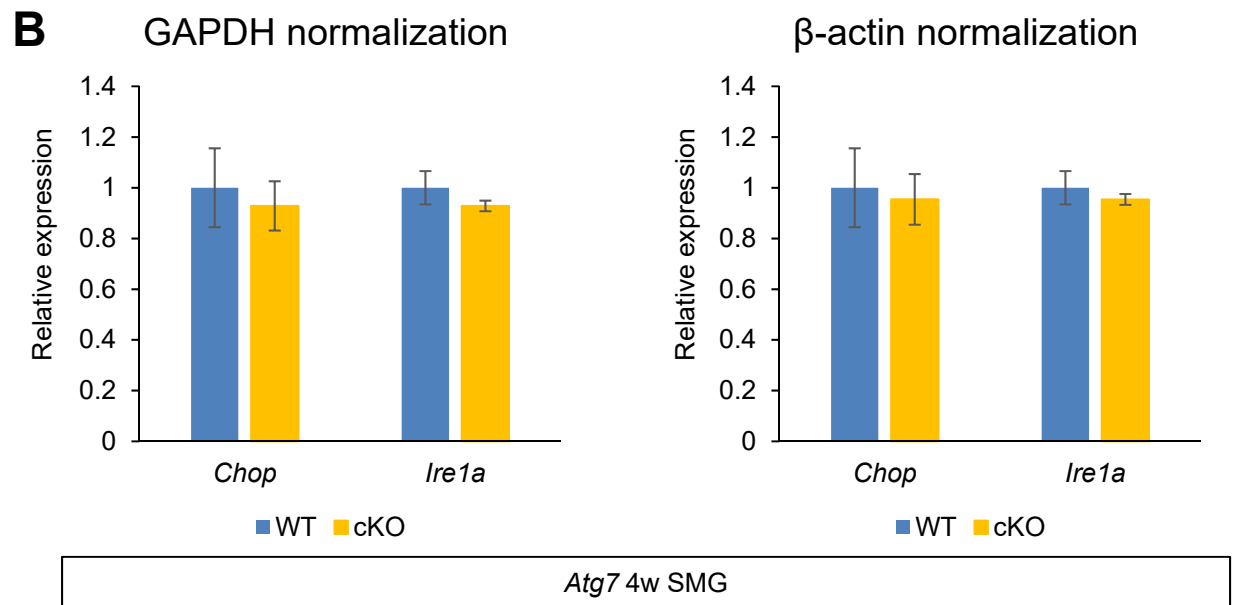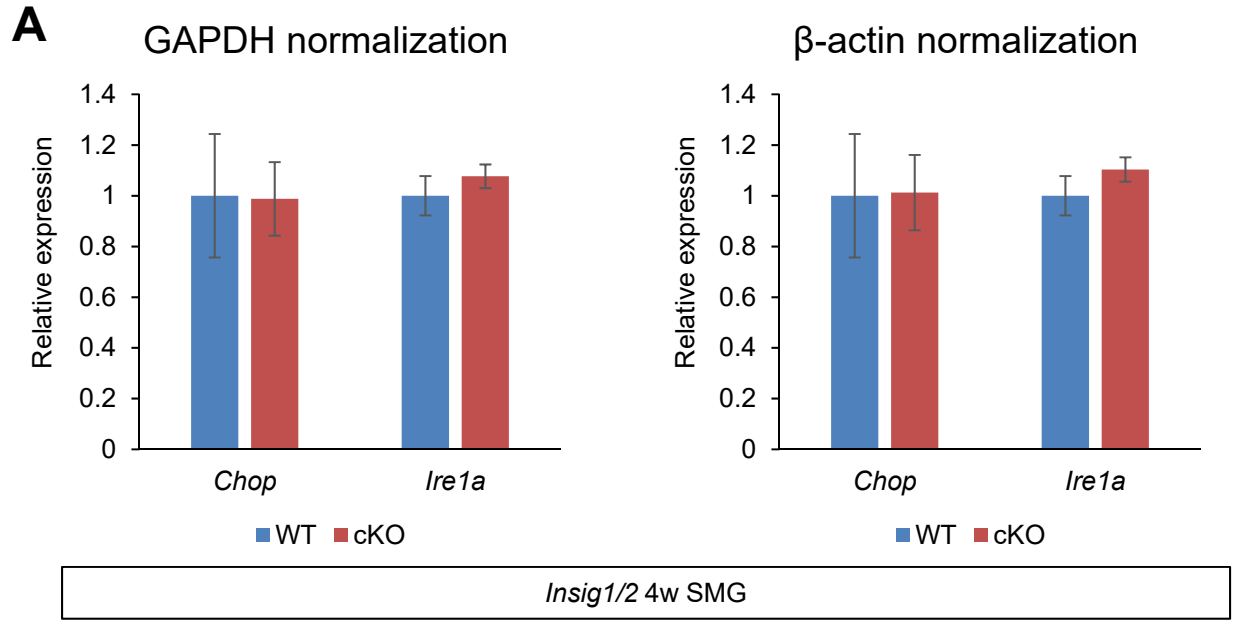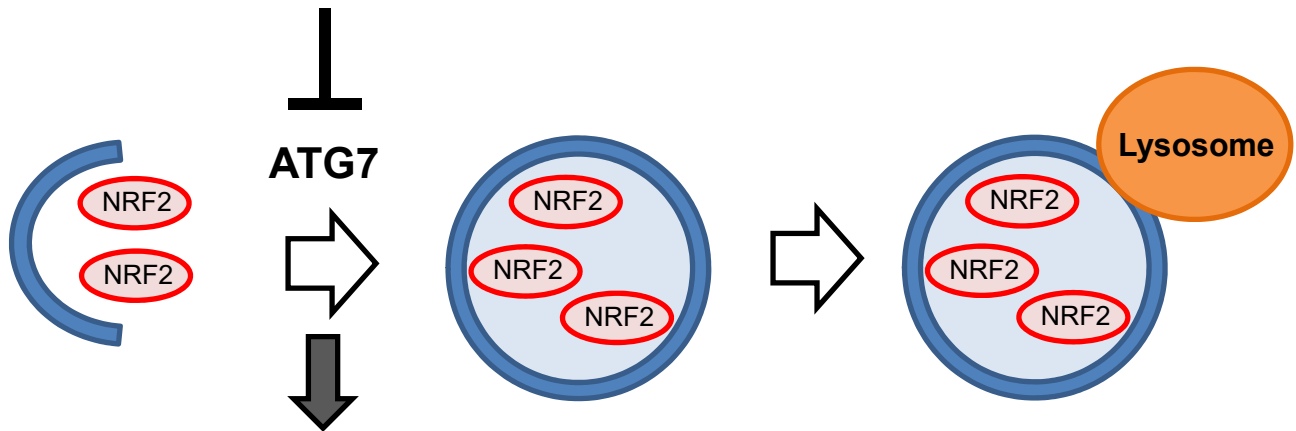
ARE site 4

```
Dog          gccctatcacacagacatctgttctcagtctcttcctctttatgatcgctacagatgacaaggg
Horse        gccctatcacacagacatctgttctcagtttcttcctctttatgatcgctacagatgacaaggg
Macaque      gccctatcacacagacatctgctctctgttgcttcctctttatggtcgctacagatgacaggag
Orangutan    gccctatcacacagacatctgttctcagtttcctcctctttgtggtcgctacagatgacaaggg
Human        gccctatcacacagacatctgctctcagtttcttcctctttgtggtcgctacagatgacaaggg
Chimpanzee   gccctatcacacagacatctgctctcagtttcttcctctttgtggtcgctacagatgacaaggg
Mouse        gccttatcacacaaacatctgcgcgcagtttcttcctctttctgatcgctgcagttgacaaggg
Rat          gccttatcacacaaacatctgcgctcagtttcttcctctttctgatcgctgcagatgacaaggg
             *** ********* *******   * * **   * ******** ** ***** *** ***** * *
                                                                   Site4
```

Fig. S14. Bioinformatics analysis for the binding sites of NRF2 (ARE) in the *Foxa1* promoter region.

Promoter sequences of the indicated binding sites that are conserved in all eight species are highlighted in green.
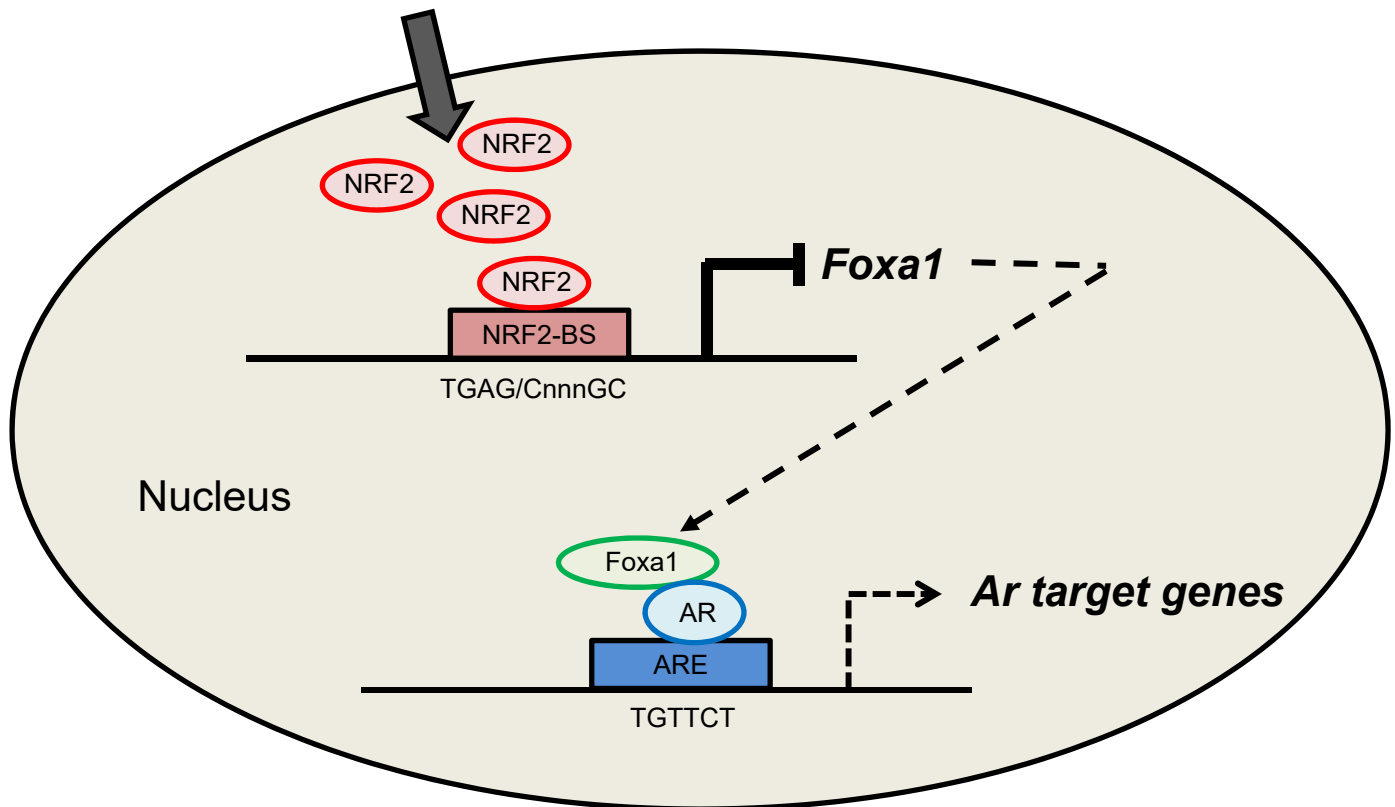
Fig. S15. Model of the androgen pathway activation through cholesterol and autophagy.

Excessive cholesterol level suppresses *Atg7* expression in ducts of the salivary glands, which in turn results in the accumulation and translocation of NRF2 into the nucleus. NRF2 suppresses expression of *Foxa1*, which supports AR binding to the androgen-response element (ARE) by opening chromatin and recruiting AR to the ARE. Therefore, *Foxa1* expression is decreased in the salivary glands of *Insig1/2* cKO and *Atg7* cKO mice. Since the complex of transcription factors FOXA1 and AR induces gene expression of *Ar* targets, decreased *Foxa1* expression results in decreased AR signaling.

Table S1. Antibodies used in this study.

Antibody name	Provider	Catalog number	Application	Final Concentration
α-SMA	Abcam	ab5694	IHC	1:100
AQP5	Alomone labs	AQP-005	IHC	1:100
Androgen receptor (AR)	Abcam	ab133273	IHC	1:100
ATG7	Cell Signaling Technology	2631	WB	1:1000
c-KIT	Cell Signaling Technology	3074	IHC	1:100
EGF	Abcam	ab9695	IHC	1:100
FOXA1	Abcam	ab170933	IHC	1:100
GAPDH	Millipore	MAB374	WB	1:6000
Histone H3	Cell Signaling Technology	9715	WB	1:1000
HMGCR	Santa Cruz	sc-33827	WB	1:1000
INSIG1	Abcam	ab70784	WB	1:500
INSIG2	Abcam	ab86415	WB	1:500
Ki67	Abcam	ab16667	IHC	1:100
KRT17/19	Cell Signaling Technology	12434	IHC	1:100
LAMP2	Abcam	ab203224	IHC	1:100
LC3B	Cell Signaling Technology	2775	IHC	1:100
			WB	1:1000
MIST1	Cell Signaling Technology	14896	IHC	1:100
NGF	Abcam	ab6199	IHC	1:100
NRF2	Abcam	ab62352	IHC	1:100
			ChIP	5 µg
p62/SOSTM1	Abcam	ab56416	IHC	1:100
			WB	1: 1000

SREBP1	Novus Biologicals	NB600-582	WB	1:1000
	Santa Cruz Biotechnology	sc-13551 X	ChIP	5 μg
SREBP2	Novus Biologicals	NB100-74543	WB	1:1000
	Santa Cruz Biotechnology	sc-1352 X	ChIP	5 μg
Ubiquitin	Dako	Z0458	IHC	1:100
			WB	1: 1000
Mouse IgG, Biotinylated	Vector laboratories	BA-9200	IHC	1: 300
Rabbit IgG, Biotinylated	Vector laboratories	BA-1000	IHC	1: 1000
Mouse IgG, Alexa Fluor 488	Thermo Fisher	A-11001	IHC	1:500
Mouse IgG, Alexa Fluor 568	Thermo Fisher	A-11004	IHC	1:500
Rabbit IgG, Alexa Fluor 488	Thermo Fisher	A-11008	IHC	1:500
Mouse IgG, HRP-linked	Cell Signaling Technology	7976	WB	1: 50000
Rabbit IgG, HRP-linked	Cell Signaling Technology	7074	WB	1: 50000